Monthly Notices
of the
ROYAL ASTRONOMICAL SOCIETY

MNRAS **457,** 1037–1061 (2016) doi:10.1093/mnras/stw013

Can non-ideal magnetohydrodynamics solve the magnetic braking catastrophe?

James Wurster,[1]★ Daniel J. Price[1] and Matthew R. Bate[1,2]

[1]*Monash Centre for Astrophysics and School of Physics and Astronomy, Monash University, VIC 3800, Australia*
[2]*School of Physics, University of Exeter, Stocker Rd, Exeter EX4 4QL, UK*

Accepted 2015 December 31. Received 2015 December 22; in original form 2015 June 5

ABSTRACT

We investigate whether or not the low ionization fractions in molecular cloud cores can solve the 'magnetic braking catastrophe', where magnetic fields prevent the formation of circumstellar discs around young stars. We perform three-dimensional smoothed particle non-ideal magnetohydrodynamics (MHD) simulations of the gravitational collapse of one solar mass molecular cloud cores, incorporating the effects of ambipolar diffusion, Ohmic resistivity and the Hall effect alongside a self-consistent calculation of the ionization chemistry assuming 0.1 μm grains. When including only ambipolar diffusion or Ohmic resistivity, discs do not form in the presence of strong magnetic fields, similar to the cases using ideal MHD. With the Hall effect included, disc formation depends on the direction of the magnetic field with respect to the rotation vector of the gas cloud. When the vectors are aligned, strong magnetic braking occurs and no disc is formed. When the vectors are anti-aligned, a disc with radius of 13 au can form even in strong magnetic when all three non-ideal terms are present, and a disc of 38 au can form when only the Hall effect is present; in both cases, a counter-rotating envelope forms around the first hydrostatic core. For weaker, anti-aligned fields, the Hall effect produces massive discs comparable to those produced in the absence of magnetic fields, suggesting that planet formation via gravitational instability may depend on the sign of the magnetic field in the precursor molecular cloud core.

Key words: magnetic fields – MHD – methods: numerical – stars: formation.

1 INTRODUCTION

The 'magnetic braking catastrophe' refers to the failure of numerical star formation calculations to produce rotationally supported Keplerian discs when magnetic fields of strengths comparable to those observed in molecular clouds (e.g. Heiles & Crutcher 2005) are accounted for. This has been found in analytic studies (Allen, Li & Shu 2003; Galli et al. 2006), axisymmetric numerical models (Mellon & Li 2008) and in 3D calculations using ideal magnetohydrodynamics (MHD) (Price & Bate 2007; Hennebelle & Fromang 2008; Duffin & Pudritz 2009; Hennebelle & Ciardi 2009; Commerçon et al. 2010; Seifried et al. 2011). By contrast, recent observations suggest the presence of massive, 50–100 au discs and evidence for associated outflows in the earliest (Class 0) stages of star formation around both low- and high-mass stars (e.g. Dunham et al. 2011; Lindberg et al. 2014; Tobin et al. 2015).

Two primary solutions have been proposed: turbulence and non-ideal MHD. Seifried et al. (2012) showed in calculations of the collapse of a massive 100 $M_\odot$ core, that 100 au-scale disc formation in the presence of strong magnetic fields was indeed possible, with some argument over whether this is caused by turbulent reconnection (Santos-Lima, de Gouveia Dal Pino & Lazarian 2012, 2013) or another mechanism (Seifried et al. 2013; Li et al. 2014). Joos et al. (2013) found, using simulations of collapsing 5 $M_\odot$ cores, that turbulence diffuses the strong magnetic field out of the inner regions of the core, and that the non-zero angular momentum of the turbulence causes a misalignment between the rotation axis and the magnetic field. Both of these effects reduce the magnetic braking, and allow a massive disc to form. However, their turbulent discs remain smaller than the discs formed without magnetic fields.

The other possible solution is to include non-ideal MHD, which is the focus of our study. The initial studies all assumed ideal MHD: the gas is fully ionized with the ions and electrons being tied to the magnetic field lines. This has been known to be a poor approximation to the true conditions in molecular cloud cores since at least Mestel & Spitzer (1956). Detailed models for the ionization fraction in dense cores find values as low as $n_e/n_{H_2} = 10^{-14}$ (Nakano & Umebayashi 1986; Umebayashi & Nakano 1990, our Fig. 1). Partial ionization leads to three main non-ideal MHD effects: *Ohmic resistivity* (drift between electrons and ions/neutrals; neither ions nor electrons are tied to the magnetic field), the *Hall effect* (ion–electron drift; only

★ E-mail: james.wurster@monash.edu

electrons are tied to the magnetic field) and *ambipolar diffusion* (ion–neutral drift; both ions and electrons are tied to the magnetic field). The relative importance of each of these depends, amongst other things, on the gas density and magnetic field strength (e.g. Wardle & Ng 1999; Nakano, Nishi & Umebayashi 2002; Tassis & Mouschovias 2007; Wardle 2007; Pandey & Wardle 2008; Keith & Wardle 2014), with Wardle (2007) suggesting a steady progression through ambipolar, Hall and Ohmic-dominated regimes as gravitational collapse proceeds.

Shu et al. (2006) found that adding a constant Ohmic resistivity indeed re-enabled Keplerian disc formation in their self-similar analytic study, but found that an anomalously high resistivity ($\eta \sim 10^{22}\,\mathrm{cm^2\,s^{-1}}$) was required; this is around two orders of magnitude higher than the microscopic value (see bottom panel of Fig. 1). Krasnopolsky, Li & Shang (2010) were able to reduce the amount of resistivity required by making different assumptions, but the required resistivity is still uncomfortably high. Correspondingly, numerical simulations with Ohmic diffusion show only small, au-scale discs (Dapp & Basu 2010; Machida, Inutsuka & Matsumoto 2011; Tomida et al. 2013). Similarly, a number of authors have concluded that ambipolar diffusion alone is unable to sufficiently weaken the magnetic braking to allow large, rotationally supported discs to form under realistic conditions (Duffin & Pudritz 2009; Mellon & Li 2009; Li, Krasnopolsky & Shang 2011; Dapp, Basu & Kunz 2012; Tomida, Okuzumi & Machida 2015; Tsukamoto et al. 2015a).

The Hall effect differs from both Ohmic resistivity and ambipolar diffusion since it is not dissipative (rather it introduces a new wave, the whistler mode) and is the only effect which is sensitive to the direction of the magnetic field. The fast time-scale associated with the whistler wave makes the Hall effect difficult to model numerically (see Section 2.5), so it is usually neglected in numerical simulations. Instead, Braiding & Wardle (2012a,b) presented similarity solutions to the MHD equations for rotating, isothermal gravitational collapse. They concluded that, although the Hall effect was not the dominant term in their calculations, it was the determining factor between a solution yielding a disc with a realistic surface density or a disc with a surface density much lower than required for fragmentation and planet formation. The only difference between the two extremes was the direction of the magnetic field with respect to the rotation vector. In a related study using idealized calculations Krasnopolsky, Li & Shang (2011), showed that the Hall effect could indeed enable the formation of ∼10 au discs depending on the sign of the magnetic field.

Here, we evaluate the influence of all three non-ideal MHD effects, including the Hall effect, on the formation of discs, using 3D non-ideal self-gravitating smoothed particle magnetohydrodynamics (SPMHD) simulations of collapsing, low-mass cores, following the original ideal MHD study of Price & Bate (2007, hereafter PB07). We present the numerical formulation in Section 2, including the self-consistent ionization calculations (Section 2.2). Our initial conditions are given in Section 3. Results are presented in Section 4, with discussion and conclusions in Section 5.

2 NUMERICAL METHOD

2.1 Non-ideal MHD

We solve the equations of self-gravitating, non-ideal MHD given by

$$\frac{\mathrm{d}\rho}{\mathrm{d}t} = -\rho\nabla\cdot\boldsymbol{v}, \tag{1}$$

$$\frac{\mathrm{d}\boldsymbol{v}}{\mathrm{d}t} = -\frac{1}{\rho}\nabla\left[\left(P+\frac{1}{2}B^2\right)\mathbf{I}-\boldsymbol{B}\boldsymbol{B}\right]-\nabla\Phi, \tag{2}$$

$$\frac{\mathrm{d}\boldsymbol{B}}{\mathrm{d}t} = (\boldsymbol{B}\cdot\nabla)\,\boldsymbol{v}-\boldsymbol{B}\,(\nabla\cdot\boldsymbol{v})+\left.\frac{\mathrm{d}\boldsymbol{B}}{\mathrm{d}t}\right|_{\text{non-ideal}}, \tag{3}$$

$$\nabla^2\Phi = 4\pi G\rho, \tag{4}$$

where $\frac{\mathrm{d}}{\mathrm{d}t}\equiv\frac{\partial}{\partial t}+\boldsymbol{v}\cdot\nabla$ is the Lagrangian derivative, ρ is the density, $\boldsymbol{v}$ is the velocity, P the hydrodynamic pressure, $\boldsymbol{B}$ is the magnetic field, Φ is the gravitational potential and $\mathbf{I}$ is the identity matrix. The magnetic field has been normalized such that the Alfvén velocity is defined as $v_\mathrm{A}\equiv B/\sqrt{\rho}$ in code units. The equation set is closed by the barotropic equation of state,

$$P=\begin{cases} c_{\mathrm{s},0}^2\rho; & \rho<\rho_\mathrm{c},\\ c_{\mathrm{s},0}^2\rho_\mathrm{c}\,(\rho/\rho_\mathrm{c})^{7/5}; & \rho_\mathrm{c}\le\rho<\rho_\mathrm{d},\\ c_{\mathrm{s},0}^2\rho_\mathrm{c}\,(\rho_\mathrm{d}/\rho_\mathrm{c})^{7/5}\,(\rho/\rho_\mathrm{d})^{11/10}; & \rho\ge\rho_\mathrm{d}, \end{cases} \tag{5}$$

where $c_{\mathrm{s},0}$ is the initial isothermal sound speed, $\rho_\mathrm{c}=10^{-14}$ and $\rho_\mathrm{d}=10^{-10}\,\mathrm{g\,cm^{-3}}$. Although we do not employ full radiation MHD, the barotropic equation of state is designed to mimic the evolution of the equation of state in molecular clouds (Larson 1969; Masunaga & Inutsuka 2000; Machida, Inutsuka & Matsumoto 2008a).

These threshold densities, ρ_c and ρ_d, are the same as used in Price, Tricco & Bate (2012) and Lewis, Bate & Price (2015). The chosen value of ρ_c is lower than physically motivated in order to artificially heat the disc that forms to prevent it from fragmenting. The value of ρ_d is also lower than physically motivated based on the temperature at which the second collapse should start, but it will not affect our results since our densities seldom reach values greater than ρ_d due to our threshold for sink particle creation (see Section 3). We explicitly caution that these threshold densities are not satisfactory to study the second collapse, but sink particles are inserted prior to the onset of the second collapse.

In the given equation of state, the pressure is continuous across density thresholds. However, since the exponent on ρ changes at these densities, the local sound speed and temperature, c_s and T, respectively, will be discontinuous. See Appendix A1 for further discussion.

The non-ideal MHD term in (3) is the sum of the Ohmic resistivity (OR), the Hall effect (HE) ambipolar diffusion (AD) terms, which are given by

$$\left.\frac{\mathrm{d}\boldsymbol{B}}{\mathrm{d}t}\right|_\mathrm{OR} = -\nabla\times[\eta_\mathrm{OR}(\nabla\times\boldsymbol{B})], \tag{6}$$

$$\left.\frac{\mathrm{d}\boldsymbol{B}}{\mathrm{d}t}\right|_\mathrm{HE} = -\nabla\times\left[\eta_\mathrm{HE}\,(\nabla\times\boldsymbol{B})\times\hat{\boldsymbol{B}}\right], \tag{7}$$

$$\left.\frac{\mathrm{d}\boldsymbol{B}}{\mathrm{d}t}\right|_\mathrm{AD} = \nabla\times\left\{\eta_\mathrm{AD}\left[(\nabla\times\boldsymbol{B})\times\hat{\boldsymbol{B}}\right]\times\hat{\boldsymbol{B}}\right\}. \tag{8}$$

The general form of the resistivity coefficients (Wardle 2007) is given by

$$\eta_\mathrm{OR} = \frac{c^2}{4\pi\sigma_\mathrm{O}}, \tag{9}$$

$$\eta_\mathrm{HE} = \frac{c^2}{4\pi\sigma_\perp}\frac{\sigma_\mathrm{H}}{\sigma_\perp}, \tag{10}$$

$$\eta_{\rm AD} = \frac{c^2}{4\pi\sigma_\perp}\frac{\sigma_{\rm P}}{\sigma_\perp} - \eta_{\rm OR} = \frac{c^2}{4\pi\sigma_{\rm O}}\frac{\sigma_{\rm O}\sigma_{\rm P} - \sigma_\perp^2}{\sigma_\perp^2}, \tag{11}$$

where c is the speed of light, and σ are the conductivities, which will be calculated in Section 2.3. The use of the magnetic unit vector, $\hat{\boldsymbol{B}}$, in (7) and (8) is to ensure that all three coefficients have units of area per time. As will be shown in the next two sections, the value of η depends on the microphysics of the model, and $\eta_{\rm HE}$ can be either positive or negative, whereas $\eta_{\rm OR}$ and $\eta_{\rm AD}$ are positive (e.g. Wardle & Ng 1999). Moreover, since $(\nabla \times \boldsymbol{B}) \times \boldsymbol{B}$ is perpendicular to $\nabla \times \boldsymbol{B}$, the Hall effect is non-dissipative and breaks the degeneracy between left and right polarized Alfvén waves (e.g. Bai 2014). To calculate the conductivities, the number densities and charges of all non-neutral species are required, which we calculate in the following section.

2.2 Ionization

In ideal MHD, infinite conductivity is assumed, and the magnetic field lines are frozen into the fluid. However, in a partially ionized plasma, diffusion of the field occurs through the relative motions of the neutral and charged particles. We assume a partially ionized plasma containing four species: neutral gas, electrons, ions and (charged) dust grains, denoted by subscripts n, e, i and g, respectively. The particle masses we choose are

$$m_{\rm n} = \frac{4\,m_{\rm p}}{2X + Y},$$
$$m_{\rm i} = 24.3\,m_{\rm p},$$
$$m_{\rm g} = \frac{4}{3}\pi a_{\rm g}^3 \rho_{\rm b},$$

where $m_{\rm p}$ is the mass of a proton, $m_{\rm n} \approx 2.38\,m_{\rm p}$ using hydrogen and helium mass fractions of $X = 0.70$ and $Y = 0.28$, respectively, $m_{\rm i}$ is the mass of magnesium (e.g. Asplund et al. 2009), and $m_{\rm g} \approx 7.51 \times 10^9\,m_{\rm p}$ using a grain radius and grain bulk density of $a_{\rm g} = 0.1\,\mu$m and $\rho_{\rm b} = 3$ g cm^{-3}, respectively (Pollack et al. 1994).

Further, we assume the strong coupling approximation, which allows the medium to be treated using the single fluid approximation. In this approximation, ion pressure and momentum are negligible compared to that of the neutrals, i.e. $\rho \sim \rho_{\rm n}$ and $\rho_{\rm i} \ll \rho$, where ρ, $\rho_{\rm n}$ and $\rho_{\rm i}$ are the total, neutral and ion mass densities, respectively.

The electron charge is $Z_{\rm e} \equiv -1$ and we assume the ion charge is $Z_{\rm i} = 1$. For charge neutrality, we require

$$n_{\rm i} - n_{\rm e} + Z_{\rm g} n_{\rm g} = 0, \tag{12}$$

where we allow $Z_{\rm g}$ to be a real number rather than an integer. In general, $Z_{\rm g} < 0$.

The grain number density is proportional to the total number density, n (Keith & Wardle 2014), according to

$$n_{\rm g} = \frac{m_{\rm n}}{m_{\rm g}} f_{\rm dg} n, \tag{13}$$

where $f_{\rm dg} = 0.01$ is the dust-to-gas mass ratio (Pollack et al. 1994). For simplicity, we adopt a single-sized grain model. The electron and ion number densities vary as (e.g. Umebayashi & Nakano 1980; Fujii, Okuzumi & Inutsuka 2011)

$$\frac{{\rm d}n_{\rm i}}{{\rm d}t} = \zeta n - k_{\rm ei} n_{\rm i} n_{\rm e} - k_{\rm ig} n_{\rm i} n_{\rm g}, \tag{14}$$

$$\frac{{\rm d}n_{\rm e}}{{\rm d}t} = \zeta n - k_{\rm ei} n_{\rm i} n_{\rm e} - k_{\rm eg} n_{\rm e} n_{\rm g}, \tag{15}$$

where ζ is the ionization rate and k_{ij} are the charge capture rates.[1] Following Keith & Wardle (2014), we assume that recombination is inefficient such that the charge capture by grains dominates (i.e. $k_{\rm ei} = 0$), and that we have an approximately steady-state system (i.e. $\frac{{\rm d}n_{\rm i}}{{\rm d}t} \approx \frac{{\rm d}n_{\rm e}}{{\rm d}t} \approx 0$). This yields ion and electron number densities of

$$n_{\rm i} = \frac{\zeta n}{k_{\rm ig} n_{\rm g}}, \tag{16}$$

$$n_{\rm e} = \frac{\zeta n}{k_{\rm eg} n_{\rm g}}, \tag{17}$$

respectively. For $Z_{\rm g} < 0$, the charge capture rates for neutral grains are (Fujii et al. 2011)

$$k_{\rm ig} = \pi a_{\rm g}^2 \sqrt{\frac{8k_{\rm B}T}{\pi m_{\rm i}}}\left(1 - \frac{e^2 Z_{\rm g}}{a_{\rm g} k_{\rm B} T}\right), \tag{18}$$

$$k_{\rm eg} = \pi a_{\rm g}^2 \sqrt{\frac{8k_{\rm B}T}{\pi m_{\rm e}}}\exp\left(\frac{e^2 Z_{\rm g}}{a_{\rm g} k_{\rm B} T}\right), \tag{19}$$

where $k_{\rm B}$ is the Boltzmann constant, e is the electron charge and T is the gas temperature. For a given n and T and assuming charge neutrality (equation 12), we can construct an equation that is only dependent on $Z_{\rm g}$:

$$Z_{\rm g} = \frac{\zeta n}{n_{\rm g}^2}\left[\frac{1}{k_{\rm ig}(Z_{\rm g})} - \frac{1}{k_{\rm eg}(Z_{\rm g})}\right],$$
$$= \frac{\zeta}{n}\left(\frac{m_{\rm g}}{f_{\rm dg} m_{\rm n}}\right)^2\left[\frac{1}{k_{\rm ig}(Z_{\rm g})} - \frac{1}{k_{\rm eg}(Z_{\rm g})}\right]. \tag{20}$$

The grain charge can then be calculated by solving (20) using the Newton–Raphson method. Finally, the neutral number density is given by

$$n_{\rm n} = \frac{1}{m_{\rm n}}[\rho - (n_{\rm i} m_{\rm i} + n_{\rm e} m_{\rm e})]. \tag{21}$$

The grain charge, ion and electron number densities are almost directly proportional to the ionization rate, ζ. However, the values of ζ span a range of several orders of magnitude depending on the ionizing source. If the ionization is from the decaying radionuclides from ^{26}Al, then $\zeta = 7.6 \times 10^{-19}$ s^{-1} (Umebayashi & Nakano 2009). Canonically, if the ionization is from cosmic rays or X-rays, then the rate is $\zeta \lesssim 10^{-17}$ and $\lesssim 10^{-18}$ s^{-1}, respectively, and decreases with the depth the rays penetrate into the cloud (cf. Keith & Wardle 2014). However, recent studies have shown that, depending on environment, the rate can be even larger, $\sim 10^{-16}$ s^{-1} (Morales Ortiz et al. 2014). For our study, a fiducial value of $\zeta = 10^{-17}$ s^{-1} will be used, but the effect of decreasing the rate to 10^{-18} s^{-1} will also be studied; the former value was used in the study by Wardle & Ng (1999).

The top two panels of Fig. 1 show the grain charge and species number densities, respectively. In both panels, the solid (dashed) lines are for values using $\zeta = 10^{-17}$ (10^{-18}) s^{-1}. The discontinuities at $\rho_{\rm n} = 10^{-14}$ and 10^{-10} g cm^{-3} correspond to the discontinuities in temperature caused by the assumed equation of state.

For all densities, $-1 < Z_{\rm g} < 0$, with $Z_{\rm g} \to 0$ for increasing $n_{\rm n}$. The value of ζ is important at moderate number densities,

[1] Keith & Wardle (2014) use this form of (14) and (15), whereas Fujii et al. (2011) use $n_{\rm n}$ rather than n. Given $n_{\rm n} \sim n$, we will use the given form for numerical simplicity.

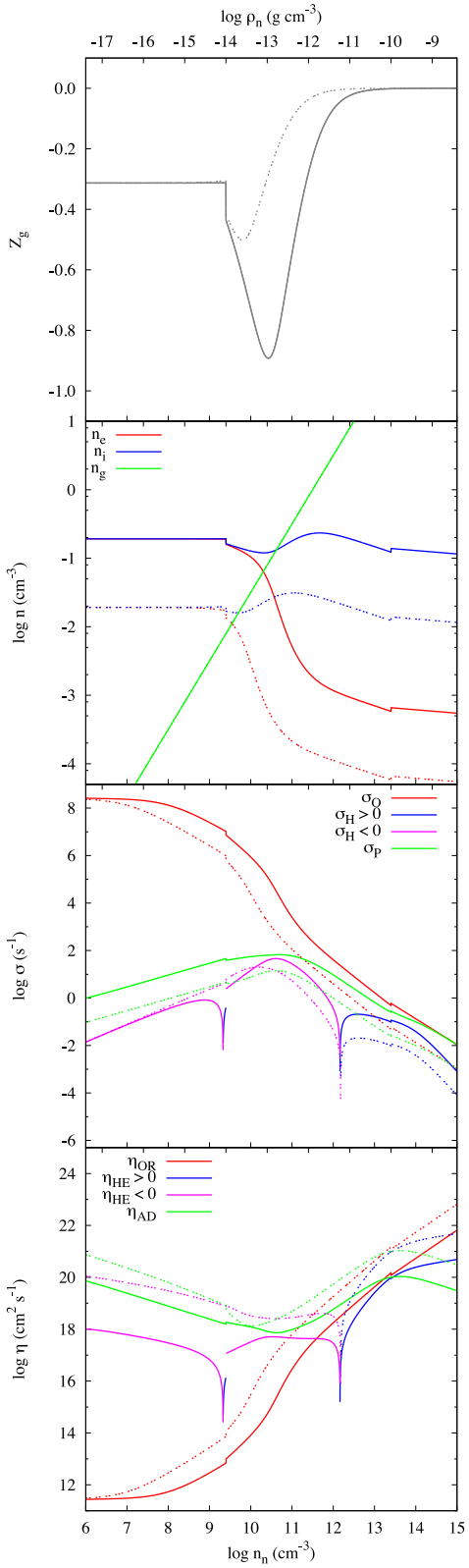

Figure 1. Top to bottom: grain charge, charged species number densities, conductivities and resistivity coefficients, using $\zeta = 10^{-17}$ (solid lines) and 10^{-18} s^{-1} (dashed lines). The top ticks on each panel correspond to mass density (top scale), and the bottom ticks correspond to number density (bottom scale). The discontinuities at $\rho_n = 10^{-14}$ and 10^{-10} g cm^{-3} correspond to the discontinuities in temperature caused by the assumed equation of state.

$2 \times 10^9 \lesssim n_n/\mathrm{cm}^{-3} \lesssim 10^{13}$, where the absolute difference between grain charges is the highest. At high densities, the relative difference in grain charge is the highest (i.e. being the same as the relative difference between the ζ's), but since these values are near zero, the exact value of ζ is not important.

In our calculations, the grain number density is directly proportional to the total number density and is independent of the ionization rate. For $n_n \lesssim 10^{10}$ cm^{-3}, n_g is similar to the values presented in Umebayashi & Nakano (1990), but above this threshold, n_g levels off for Umebayashi & Nakano (1990) who calculate the number density using a full treatment of the reaction rates of several different molecules. Ion and electron number densities follow a similar trend to that presented in the top panel of fig. 1 of Wardle & Ng (1999). Our values differ quantitatively to their results due to the differences in our parameters, the choice of equation of state, and that Wardle & Ng (1999) used the grain densities from Umebayashi & Nakano (1990) rather than $n_g \propto n$. We briefly analyse the isothermal equation of state in Appendix A2, and the barotropic equation of state with $\rho_c = 10^{-13}$ g cm^{-3} in Appendix A3. In general, the ion and electron number densities are proportional to the ionization rate, with an exception at moderate number densities; this is the same range over which the value of ζ has the largest absolute effect on the grain charge.

2.3 Conductivities

For a charged species, i.e. $j \in \{\mathrm{e}, \mathrm{i}, \mathrm{g}\}$, the relative magnitude between the magnetic forces and neutral drag describe the behaviour of the species. This relation is given by the Hall parameter, whose general form is

$$\beta_j = \frac{|Z_j| e B}{m_j c} \frac{1}{\nu_{jn}}, \tag{22}$$

where Z_j and m_j are the charge[2] and mass of species j, respectively, B is the magnitude of the magnetic field and ν_{jn} is the plasma–neutral collision frequency; the Hall parameter also represents the ratio between the gyrofrequency and the neutral collision frequency (e.g. Wardle 2007). We have slightly modified the Hall parameter such that

$$\beta_\mathrm{e} = \frac{|Z_\mathrm{e}| e B}{m_\mathrm{e} c} \frac{1}{\nu_\mathrm{en} + \nu_\mathrm{ei}}, \tag{23a}$$

$$\beta_\mathrm{i} = \frac{|Z_\mathrm{i}| e B}{m_\mathrm{i} c} \frac{1}{\nu_\mathrm{in} + \nu_\mathrm{ie}}. \tag{23b}$$

With these modifications, we can recover η_OR from Pandey & Wardle (2008) and Keith & Wardle (2014) under the assumption $\beta_\mathrm{i} \ll \beta_\mathrm{e}$. Appendix B examines the effect of modifying the Hall parameter.

The Hall parameter can be used to characterize different regimes where different effects are dominant. Given the typical value of $\beta_\mathrm{e}/\beta_\mathrm{i} \sim 1000$, Wardle (2007) defines three regimes:

$\beta_\mathrm{i} \ll \beta_\mathrm{e} \ll 1$: Ohmic resistivity

$\beta_\mathrm{i} \ll 1 \ll \beta_\mathrm{e}$: Hall effect

$1 \ll \beta_\mathrm{i} \ll \beta_\mathrm{e}$: ambipolar diffusion.

[2] Note that some authors use a β that includes the sign of Z; their conductivities, σ, are then modified accordingly.

The collisional frequencies, ν, are empirically calculated rates. The electron–ion rate is given by (Pandey & Wardle 2008)

$$\nu_{\rm ei} = 51 \ {\rm s}^{-1} \left(\frac{n_{\rm e}}{{\rm cm}^{-3}}\right) \left(\frac{T}{\rm K}\right)^{-3/2}. \tag{24}$$

The ion–electron rate is given by $\nu_{\rm ie} = \frac{\rho_{\rm e}}{\rho_{\rm i}} \nu_{\rm ei}$. The plasma–neutral collisional frequency is given by

$$\nu_{j{\rm n}} = \frac{\langle \sigma v \rangle_{j{\rm n}}}{m_{\rm n} + m_j} \rho_{\rm n}, \tag{25}$$

where $\langle \sigma v \rangle_{j{\rm n}}$ is the rate coefficient for the momentum transfer by the collision of particle of type j with the neutrals. For electron–neutral collisions, it is assumed that the neutrals are comprised of hydrogen and helium, such that the rate coefficient is

$$\langle \sigma v \rangle_{\rm en} = X \langle \sigma v \rangle_{\rm e\text{-}H_2} + Y \langle \sigma v \rangle_{\rm e\text{-}He}. \tag{26}$$

Following Pinto & Galli (2008), we use

$$\langle \sigma v \rangle_{\rm e\text{-}H_2} = 3.16 \times 10^{-11} \ {\rm cm}^3 \ {\rm s}^{-1} \left(\frac{v_{\rm rms}}{\rm km \ s^{-1}}\right)^{1.3},$$

$$\langle \sigma v \rangle_{\rm e\text{-}He} = 7.08 \times 10^{-11} \ {\rm cm}^3 \ {\rm s}^{-1} \left(\frac{v_{\rm rms}}{\rm km \ s^{-1}}\right),$$

with

$$v_{\rm rms} = \sqrt{v_{\rm d}^2 + \frac{8 k_{\rm B} T}{\pi \mu_{\rm en}}}, \tag{27}$$

where $v_{\rm d}$ is the drift velocity between the electron and the neutral, and $\mu_{\rm en}$ is the reduced mass of the electron–neutral pair; we assume $v_{\rm d} = 0$ and $\mu_{\rm en} \approx m_{\rm e}$. The ion–neutral rate is (Pinto & Galli 2008)

$$\langle \sigma v \rangle_{\rm in} = 2.81 \times 10^{-9} \ {\rm cm}^3 \ {\rm s}^{-1} \ Z_{\rm i}^{1/2} \times \left[X \left(\frac{p_{\rm H_2}}{\text{Å}^3}\right)^{1/2} \left(\frac{\mu_{\rm i\text{-}H_2}}{m_{\rm p}}\right)^{-1/2} + Y \left(\frac{p_{\rm He}}{\text{Å}^3}\right)^{1/2} \left(\frac{\mu_{\rm i\text{-}He}}{m_{\rm p}}\right)^{-1/2} \right], \tag{28}$$

where the values of polarizability are $p_{\rm H_2} = 0.804 \ \text{Å}^3$ and $p_{\rm He} = 0.207 \ \text{Å}^3$ (Osterbrock 1961).

For grain–neutral collisions, the rate coefficient is given by (Wardle & Ng 1999; Pinto & Galli 2008)

$$\langle \sigma v \rangle_{\rm gn} = \pi a_{\rm g}^2 \delta_{\rm gn} \sqrt{\frac{128 k_{\rm B} T}{9 \pi m_{\rm n}}}, \tag{29}$$

where $\delta_{\rm gn}$ is the Epstein coefficient. From experiments with micron-sized melamine–formaldehyde spheres, $\delta_{\rm gn} \approx 1.3$ (Liu et al. 2003).

The Ohmic, Hall and Pedersen conductivities can now be calculated (e.g. Wardle & Ng 1999; Wardle 2007) viz.

$$\sigma_{\rm O} = \frac{ec}{B} \sum_j n_j |Z_j| \beta_j, \tag{30}$$

$$\sigma_{\rm H} = \frac{ec}{B} \sum_j \frac{n_j Z_j}{1 + \beta_j^2}, \tag{31}$$

$$\sigma_{\rm P} = \frac{ec}{B} \sum_j \frac{n_j |Z_j| \beta_j}{1 + \beta_j^2}. \tag{32}$$

We explicitly note that $\sigma_{\rm O}$ and $\sigma_{\rm P}$ are positive, whereas $\sigma_{\rm H}$ can be positive or negative. The total conductivity perpendicular to the magnetic field is

$$\sigma_\perp = \sqrt{\sigma_{\rm H}^2 + \sigma_{\rm P}^2}. \tag{33}$$

The third panel of Fig. 1 shows the Ohmic, Hall and Pedersen conductivities for $\zeta = 10^{-17}$ (solid lines) and 10^{-18} s^{-1} (dashed lines). When a magnetic field is required in the calculation, for the purpose of illustration, we use the relation used in Wardle & Ng (1999), which follows the standard $n_{\rm n}^{1/2}$ relation for $n_{\rm n} < 10^6$ cm^{-3} (Myers & Goodman 1988) and a weaker dependence at higher densities:

$$\left(\frac{B}{\rm mG}\right) = \begin{cases} (n_{\rm n}/10^6 \ {\rm cm}^{-3})^{1/2}; & n_{\rm n} < 10^6 \ {\rm cm}^{-3} \\ (n_{\rm n}/10^6 \ {\rm cm}^{-3})^{1/4}; & \text{else} \end{cases}. \tag{34}$$

The Hall conductivity is more sensitive to the value of ζ than the other two conductivities. For both values of ζ, there is a discontinuity at $n_{\rm n} \approx 1.5 \times 10^{12}$ cm^{-3} across which the value of $\sigma_{\rm H}$ switches from negative to positive. For $\zeta = 10^{-17}$ s^{-1}, there is a small range, $2.1 \lesssim n_{\rm n}/(10^9 \ {\rm cm}^{-3}) \lesssim 2.5$, where the Hall conductivity is again positive; at the lower end of this range, the value of $\sigma_{\rm H}$ naturally switches from negative to positive, while the changeover at the upper end corresponds to the discontinuity in temperature caused by the assumed equation of state. The behaviour of the Ohmic conductivity is similar to the behaviour of the grain charge: approximately independent of ζ at low densities and proportional to it at high densities. The Pedersen conductivity is proportional to ζ, except at medium number densities. Our values of the conductivities differ from those in the bottom panel of their fig. 2 of Wardle & Ng (1999), however, different assumptions and values were used here; see Appendix A2 for further discussion.

The bottom panel of Fig. 1 shows the value of the coefficients, η, for Ohmic resistivity, the Hall effect and ambipolar diffusion for both values of ζ; the magnetic field is again given by (34). It is clear from this figure that each non-ideal MHD term is dominant at various densities, with ambipolar diffusion being the most important at low densities and Ohmic resistivity being the most important at high densities. The Hall effect has a small range of densities where it is dominant for $\zeta = 10^{-18}$ s^{-1}, but it is never the dominant effect for $\zeta = 10^{-17}$ s^{-1}. We caution that this statement is true given (34), but may not be true in general where $\boldsymbol{B}$ evolves differently to this (e.g. in our simulations). Moreover, at medium densities, two or all three effects can be simultaneously important (e.g. at $n_{\rm n} \approx 2.5 \times 10^{13}$ cm^{-3} where all three coefficients are similar). Given the range of densities in a typical star formation simulation at any given time, it is possible for different terms to dominate in different spatial regions.

2.4 Smoothed particle magnetohydrodynamics

To perform our simulations, we use the 3D SPMHD code PHANTOM with the inclusion of self-gravity. The ideal MHD equations (1)–(3) are discretized into SPMHD (see review by Price 2012) as

$$\rho_a = \sum_b m_b W_{ab}(h_a); \quad h_a = h_{\rm fac} \left(\frac{m_a}{\rho_a}\right)^{1/3}, \tag{35}$$

$$\frac{{\rm d}v_a^i}{{\rm d}t} = \sum_b m_b \left[\frac{S_a^{ij}}{\Omega_a \rho_a^2} \nabla_a^j W_{ab}(h_a) + \frac{S_b^{ij}}{\Omega_b \rho_b^2} \nabla_a^j W_{ab}(h_b) \right] - f B_a^i \sum_b m_b \left[\frac{B_a^j}{\Omega_a \rho_a^2} \nabla_a^j W_{ab}(h_a) + \frac{B_b^j}{\Omega_b \rho_b^2} \nabla_a^j W_{ab}(h_b) \right] - \nabla \Phi_a + \left.\frac{{\rm d}v_a^i}{{\rm d}t}\right|_{\rm artificial}, \tag{36}$$

$$\frac{\mathrm{d}B_a^i}{\mathrm{d}t} = -\frac{1}{\Omega_a\rho_a}\sum_b m_b\Big[v_{ab}^i B_a^j \nabla_a^j W_{ab}(h_a) - B_a^i v_{ab}^j \nabla_a^j W_{ab}(h_a)\Big] + \left.\frac{\mathrm{d}B_a^i}{\mathrm{d}t}\right|_{\rm non\text{-}ideal} + \left.\frac{\mathrm{d}B_a^i}{\mathrm{d}t}\right|_{\rm artificial}, \tag{37}$$

$$\nabla^2\Phi_a = 4\pi G\rho_a, \tag{38}$$

where we sum over all particles b within the kernel radius, W_{ab} is the smoothing kernel, $\boldsymbol{v}_{ab} = \boldsymbol{v}_a - \boldsymbol{v}_b$, Ω_a is a dimensionless correction term to account for a spatially variable smoothing length h_a (Monaghan 2002; Springel & Hernquist 2002), the stress tensor is given by

$$S^{ij} \equiv -\left(P + \frac{1}{2}B^2\right)\delta^{ij} + B^i B^j, \tag{39}$$

and $\left.\frac{\mathrm{d}v_a^i}{\mathrm{d}t}\right|_{\rm artificial}$ is the artificial viscosity, as described in Price & Federrath (2010).

Numerically, $\nabla\cdot\boldsymbol{B}$ is not exactly zero. However, this term is inherently contained in the conservative form of the momentum equation (i.e. the first line of equation 36). When $\frac{1}{2}\boldsymbol{B}^2 > P$, the inclusion of this term can trigger the tensile instability, which causes particles to unphysically clump together. To correct for this, a simple approach is to subtract the source term [i.e. the second line of equation (36) using $f = 1$; Børve, Omang & Trulsen 2001]. Since subtracting the term violates energy and momentum conservation (but only in so far as the divergence term in (36) is non-zero; e.g. Price 2012; Tricco & Price 2012), Børve, Omang & Trulsen (2004) introduced a variable f such that $0 < f < \frac{1}{2}$. However, Tricco & Price 2012 showed that numerical artefacts can be produced for $f < 1$, thus suggested $f = 1$ everywhere. Since the tensile instability is only triggered for $\frac{1}{2}\boldsymbol{B}^2 > P$, we use

$$f = \begin{cases} 1; & \beta \leq 1, \\ 2-\beta; & 1 < \beta \leq 2 \\ 0; & \beta > 2, \end{cases} \tag{40}$$

where $\beta = \frac{2P}{\boldsymbol{B}^2}$ is the plasma beta; f is calculated for each particle, a, using only the properties of particle a. This allows the source term to be removed where it is problematic, but maintains energy and momentum conservation elsewhere. The function $1 < \beta \leq 2$ allows a smooth decrease between the two extremes, and to avoid sharp jumps when $\beta \sim 1$. To avoid confusion with the Hall parameters, $\beta_{\rm e}$, $\beta_{\rm i}$ and $\beta_{\rm g}$, we will always use β with no subscript to refer to the plasma beta.

We adopt the usual cubic spline kernel, with $h_{\rm fac} = 1.2$ in (35) specifying the ratio of the smoothing length to the particle spacing, equivalent to ∼58 neighbours (Price 2012). Finally, the magnetic field has been normalized such that $v_{\rm A} \equiv B/\sqrt{\rho}$ (see Price & Monaghan 2004). We solve (38) following Price & Monaghan (2007) at short range, with a k-d tree algorithm similar to that described in Gafton & Rosswog (2011) used to compute the long-range gravitational interaction in an efficient manner.

To calculate the non-ideal MHD terms in (37), we follow the procedure described in Wurster, Price & Ayliffe (2014). First, the current density, $\boldsymbol{J} \equiv \nabla\times\boldsymbol{B}$, is calculated using the difference operator (cf. Price 2010, 2012):

$$\boldsymbol{J}_a = \frac{1}{\Omega_a\rho_a}\sum_b m_b(\boldsymbol{B}_a - \boldsymbol{B}_b)\times\nabla_a W_{ab}(h_a). \tag{41}$$

The general non-ideal MHD term is then calculated using the conjugate (i.e. symmetric) operator,

$$\left.\frac{\mathrm{d}\boldsymbol{B}_a}{\mathrm{d}t}\right|_{\rm non\text{-}ideal} = -\rho_a\sum_b m_b\left[\frac{\boldsymbol{D}_a}{\Omega_a\rho_a^2}\times\nabla_a W_{ab}(h_a) + \frac{\boldsymbol{D}_b}{\Omega_b\rho_b^2}\times\nabla_a W_{ab}(h_b)\right], \tag{42}$$

where $\boldsymbol{D}_a$ is defined for each non-ideal MHD term as

$$\boldsymbol{D}_a^{\rm OR} = -\eta_{\rm OR}\boldsymbol{J}_a, \tag{43}$$

$$\boldsymbol{D}_a^{\rm HE} = -\eta_{\rm HE}\boldsymbol{J}_a\times\hat{\boldsymbol{B}}_a, \tag{44}$$

$$\boldsymbol{D}_a^{\rm AD} = \eta_{\rm AD}\left(\boldsymbol{J}_a\times\hat{\boldsymbol{B}}_a\right)\times\hat{\boldsymbol{B}}_a. \tag{45}$$

Once $\boldsymbol{J}_a$ is calculated, $\boldsymbol{D}_a$ can be calculated without knowledge of any of particle a's neighbours. Although this algorithm is the same as in Wurster et al. (2014), here we self-consistently calculate the resistivity coefficients as described in the previous sections rather than defining them as constants for the entire simulation. Therefore, no a priori knowledge is required of which term is dominant. This algorithm has been thoroughly tested for ambipolar diffusion with constant resistivity in Wurster et al. (2014); given the non-diffusive nature of the Hall effect, we present the results from two tests in Appendix C1.

We compute the artificial resistivity term (Price & Monaghan 2004, 2005) in (37) using

$$\left.\frac{\mathrm{d}\boldsymbol{B}_a}{\mathrm{d}t}\right|_{\rm artificial} = \frac{\rho_a}{2}\sum_b m_b(\boldsymbol{B}_a - \boldsymbol{B}_b)\left[\frac{v_{{\rm sig},a}^B}{\rho_a^2}\frac{\hat{\boldsymbol{r}}_{ab}\cdot\nabla_a W_{ab}(h_a)}{\Omega_a} + \frac{v_{{\rm sig},b}^B}{\rho_b^2}\frac{\hat{\boldsymbol{r}}_{ab}\cdot\nabla_a W_{ab}(h_b)}{\Omega_b}\right], \tag{46}$$

where $v_{\rm sig}^{\rm B} = \sqrt{c_s^2 + v_{\rm A}^2}$ is the signal velocity, set to the fast magnetosonic speed. Each particle has its own $\alpha_{\rm B}$, set using the switch described in Tricco & Price (2013):

$$\alpha_{\rm B} = \min\left(\frac{h|\nabla\boldsymbol{B}|}{|\boldsymbol{B}|}, 1.0\right), \tag{47}$$

where the magnitude of the gradient matrix is computed from the 2-norm (Tricco & Price 2013). This ensures that resistivity is only strong where there are strong gradients in the magnetic field. The Ohmic diffusion resulting from the artificial resistivity term for a given particle a is given by

$$\eta_{\rm art}^a \approx \frac{1}{2}\alpha_{\rm B}^a v_{{\rm sig},a}^{\rm B} h_a. \tag{48}$$

We compute this at each step in the calculation and compare it to the physical diffusion coefficients to ensure that physical resistivity dominates.

Finally, we control the divergence of the magnetic field using the constrained hyperbolic divergence cleaning scheme described in Tricco & Price (2012). Importantly, this treatment of the magnetic field evolution is completely general as in Price et al. (2012) and Bate, Tricco & Price (2014), unlike the Euler potentials method used by PB07.

2.5 Timestepping

For non-ideal MHD, the timestep for particle a is constrained by

$$\mathrm{d}t_a < C_{\text{non-ideal}} \frac{h_a^2}{|\eta_a|}, \tag{49}$$

where $\eta_a = \max(\eta_{\text{OR},a}, \eta_{\text{HE},a}, \eta_{\text{AD},a})$ and $C_{\text{non-ideal}} < 1$ is a positive coefficient analogous to the Courant number. Wave calculations involving the whistler mode suggest $C_{\text{non-ideal}} = \frac{1}{2\pi}$ as the optimal value. This agrees with the stability test in Bai (2014), who optimally sets $C_{\text{non-ideal}} = \frac{1}{6}$. We find that values much larger than this yield unstable results.

In some cases, this timestep can be considerably smaller than the normal Courant timestep, thus can drastically slow down the simulation. For the C-shock test presented in Mac Low et al. (1995) and Wurster et al. (2014), the timestep was 30–40 times shorter for the case that included ambipolar diffusion compared to the case using ideal MHD.

For the diffusive terms that are parabolic in nature (i.e. Ohmic resistivity and ambipolar diffusion; the Hall effect is hyperbolic), we can relax the stringent condition imposed by (48) by implementing super timestepping (Alexiades, Amiez & Gremaud 1996). Super timestepping requires stability at the end of a cycle of N steps rather than at the end of every step. To implement super timestepping, we first choose timesteps such that

$$\mathrm{d}t = \min(\mathrm{d}t_{\text{Courant}}, \mathrm{d}t_{\text{HE}}), \tag{50}$$

$$\mathrm{d}t'_{\text{diff}} = \min(\mathrm{d}t_{\text{OR}}, \mathrm{d}t_{\text{AD}}), \tag{51}$$

and dictate that the simulation must be stable when it has progressed time $\mathrm{d}t$. If $\mathrm{d}t > \mathrm{d}t'_{\text{diff}}$, then the number of timesteps required to progress $\mathrm{d}t$ is $N = \text{int}(\sqrt{\frac{\mathrm{d}t}{k\mathrm{d}t'_{\text{diff}}}}) + 1$ (Choi, Kim & Wiita 2009), where $k \leq 1$ is a positive scalar; we set $k = 0.9$. We then reset the diffusive timestep to

$$\mathrm{d}t_{\text{diff}} = \frac{N^2}{k}\mathrm{d}t. \tag{52}$$

The individual sub-steps are then given by

$$\mathrm{d}\tau_j = \mathrm{d}t_{\text{diff}} \left[(\nu - 1) \cos\left(\frac{2j-1}{N} \frac{\pi}{2} \right) + \nu + 1 \right]^{-1} \tag{53}$$

for $j = 1, \ldots, N$, where $0 < \nu < 1$ is pre-calculated for a given N using the relation in (52). The full timestep, $\mathrm{d}t$, is recovered with

$$\mathrm{d}t = \sum_{j=1}^{N} \mathrm{d}\tau_j = \mathrm{d}t_{\text{diff}} \frac{N}{2\sqrt{\nu}} \left(\frac{\left(1+\sqrt{\nu}\right)^{2N} - \left(1-\sqrt{\nu}\right)^{2N}}{\left(1+\sqrt{\nu}\right)^{2N} + \left(1-\sqrt{\nu}\right)^{2N}} \right). \tag{54}$$

Given the predictor–corrector method used by PHANTOM, we decrease $\mathrm{d}t \rightarrow \mathrm{d}t/2$ if the signal velocity is predicted to increase more than 10 per cent during a given $\mathrm{d}\tau$. Although decreasing $\mathrm{d}t$ to maintain small changes in the signal velocity can counteract the benefits of super timestepping, it does provide the required stability over $\mathrm{d}t$ while allowing a decrease in runtime. In Appendix C2, we discuss super timestepping, for both test cases and our models; further tests of super timestepping can be found in Commerçon et al. (2011) and Tsukamoto, Iwasaki & Inutsuka (2013).

The Hall term is hyperbolic, thus super timestepping cannot be applied. Further, we have no explicit treatment of this term (i.e. the minimum timestep is given by equation 50), thus the Hall effect can cause a considerable slow-down in the simulations. Under certain circumstances, $\mathrm{d}t_{\text{HE}}$ can be several hundred or thousand times smaller than the Courant-limited timestep, which essentially results in the premature end of the simulation.

3 INITIAL CONDITIONS

Our setup is similar to that used in PB07. We use a spherical cloud of radius $R = 4 \times 10^{16}$ cm $= 0.013$ pc, mass $M = 1$ M$_\odot$ and mean density of $\rho_0 = 7.43 \times 10^{-18}$ g cm^{-3}. The cloud has an initial rotational velocity of $\Omega = 1.77 \times 10^{-13}$ rad s^{-1}, an initial sound speed of $c_{\text{s},0} = 2.19 \times 10^4$ cm s^{-1}, and we assume a uniform magnetic field aligned (or anti-aligned) with the axis of rotation, i.e. $B_{0,x} = B_{0,y} = 0$, $B_{0,z} \neq 0$. The free-fall time is $t_{\text{ff}} = 2.4 \times 10^4$ yr, which is the characteristic time-scale for this study.

To avoid boundary conditions at the edge of the sphere, the cloud is placed in a uniform, low-density box of edge length $l = 4R = 0.052$ pc, which is in pressure equilibrium with the cloud; the density contrast between the cloud and the surrounding medium is 30:1. This allows the cloud to be modelled self-consistently, and the large ratio ensures that the surrounding medium will not contribute significantly to the self-gravity of the cloud. We use quasi-periodic boundary conditions at the edge of the box, in which smoothed particle hydrodynamics (SPH) particles interact hydrodynamically 'across the box', but not gravitationally.

Sink particles (Bate, Bonnell & Price 1995) are introduced so that we can follow the collapse efficiently after the formation of the first hydrostatic core. When the maximum gas density surpasses $\rho_{\text{crit}} = 10^{-10}$ g cm^{-3}, the densest gas particle is replaced with a sink particle when it and its neighbours within $r_{\text{acc}} = 6.7$ au meet a given set of criteria; all the neighbours are immediately accreted on to the sink particle. Gas which later enters this radius is checked against given criteria to determine if is accreted on to the sink particle. Sink particles interact with the gas only via gravity and accretion. Thus, magnetic fields in the central regions are removed and not allowed to feed back on the surrounding material. While this is a crude approximation, it enables us to perform our study efficiently (PB07). However, sink particle boundaries with magnetic fields are problematic in SPMHD and a systematic study of alternative approaches would be worthwhile.

The parameters that govern the sink particle (i.e. the critical density, ρ_{crit} and the accretion radius, r_{acc}) must be chosen carefully since these parameters will influence the results. Objects smaller than the accretion radius are necessarily unresolved, but the density profile around the sink will also vary depending on r_{acc} since the sink effectively adds an outflow boundary condition at this radius; this can lead to the sink influencing the gas on scales larger than r_{acc} (Machida, Inutsuka & Matsumoto 2014).

Given our initial conditions and our chosen equation of state, we require at least 30 000 particles to resolve the local Jeans mass throughout the calculation (Bate & Burkert 1997; PB07). We present simulations at two different resolutions: 445 000 particles including 302 000 in the sphere, and 1484 000 particles including 1004 000 in the sphere. Thus, this resolution condition is clearly satisfied in our models. Our primary analysis of a strong magnetic field and $\zeta = 10^{-17}$ s^{-1} will be performed at the higher resolution, while, for computational efficiency, the remainder of the analyses will be performed at the lower resolution. Our included resolution studies indicate that our conclusions are independent of resolution. All particles are set up on a regular close-packed lattice (e.g. Morris 1996). All undesirable effects initially introduced by the regularity of the lattice are transient and washed out long before the star formation occurs.

Table 1. A list of the parameters varied in this study. The second column lists values of the parameter that we tested. For our initial conditions, $\mu_0 = 5$, 7.5 and 10 correspond to magnetic field strengths of $B = \{1.63, 1.09, 0.817\} \times 10^{-4}$ G, respectively. We define models listed as 'non-ideal' as containing all three non-ideal MHD terms. Unless otherwise stated, the cosmic ionization rate will be set at $\zeta = 10^{-17}$ s^{-1}.

Parameter	All values to be tested
Non-ideal MHD component	Ideal MHD, non-ideal MHD. Ohmic-only, Hall-only, ambipolar-only.
Initial mass-to-flux ratio, μ_0	5.0, 7.5, 10.0
Direction of the magnetic field	$\boldsymbol{B}_0 \cdot \boldsymbol{\Omega}_0 > 0$, $\boldsymbol{B}_0 \cdot \boldsymbol{\Omega}_0 < 0$
Cosmic ray ionization rate, ζ	10^{-17} s^{-1}, 10^{-18} s^{-1}
Resolution (particles in sphere)	$\sim 3 \times 10^5$, $\sim 10^6$

We characterize the magnetic field in terms of the normalized parameter μ, where

$$\mu \equiv \frac{M/\Phi_{\rm B}}{(M/\Phi_{\rm B})_{\rm crit}}, \tag{55}$$

where $M/\Phi_{\rm B}$ is the mass-to-flux ratio

$$\frac{M}{\Phi_{\rm B}} \equiv \frac{M}{\pi R^2 B}, \tag{56}$$

and $(M/\Phi_{\rm B})_{\rm crit}$ is the critical value where magnetic fields prevent gravitational collapse altogether

$$\left(\frac{M}{\Phi_{\rm B}}\right)_{\rm crit} = \frac{c_1}{3\pi}\sqrt{\frac{5}{G}}, \tag{57}$$

where M is the total mass contained within the cloud, $\Phi_{\rm B}$ is the magnetic flux threading the surface of the (spherical) cloud at radius R assuming a uniform magnetic field of strength B, G is the gravitational constant and $c_1 \simeq 0.53$ is a parameter numerically determined by Mouschovias & Spitzer (1976). Observations suggest $\mu \sim 2$–10 in molecular cloud cores (e.g. Crutcher 1999; Bourke et al. 2001; Heiles & Crutcher 2005); this value could be even smaller once projection effects are taken into account (Li et al. 2013).

In this study, we test the effect of the different non-ideal MHD terms, the initial mass-to-flux-ratio, μ_0, the direction of the magnetic field, the cosmic ray ionization rate and resolution. Table 1 lists these parameters, along with values to be tested. Unless otherwise stated, the cosmic ionization rate will be set at $\zeta = 10^{-17}$ s^{-1}. We define models listed as 'non-ideal' as containing all three non-ideal MHD terms.

4 RESULTS

4.1 Ideal MHD

For a baseline comparison, we present four simulations of the axisymmetric collapse of a molecular cloud core using ideal MHD. This is similar, but smaller in scope, to the study presented in PB07. Fig. 2 shows the face-on gas column density profiles for $\mu_0 = \infty$ (i.e. no magnetic fields; labelled as 'Hydro' in the figures), 10, 7.5 and 5 at five different times during the collapse; these ratios correspond to magnetic field strengths of $B = \{0, 0.817, 1.09, 1.63\} \times 10^{-4}$ G, respectively. There are initially $\sim 3 \times 10^5$ particles in the gas sphere. In Fig. 2, the cloud is initially rotating counterclockwise with the initial magnetic field directed out of the page (i.e. $\boldsymbol{B}_0 \cdot \boldsymbol{\Omega}_0 > 0$). The hydrodynamic model forms a large, massive disc. This is expected since there is no mechanism (i.e. magnetic fields) to transport the angular momentum out of the system. For the magnetic models, increasing the initial magnetic field strength (i.e. decreasing μ_0) retards the collapse; this is seen at $t = 1.01\,t_{\rm ff}$, where the central density is lower for stronger magnetic fields.

To perform a quantitative comparison, we first define the disc and the star+disc system. Gas is 'in the disc' if it has density $\rho > \rho_{\rm disc,\,min} = 10^{-13}$ g cm^{-3}, which is one order of magnitude above which the gas becomes adiabatic. The mass of the star+disc system is defined as the mass of the disc plus the mass of the sink particle, which represents the first hydrostatic core. The radius of the disc is defined as the radius in which 99 per cent mass of the star+disc system is contained (PB07). We caution that the disc characteristics are variable with time since gas is condensing on to it as well as being fed to the sink from it. Thus, the star+disc system yields a more robust analyse of mass since the mass that accretes on to the disc remains in either the disc or the sink particle. Despite its temporal variability, the disc properties will be analysed since whether or not a disc forms is the focus of this study.

The left-hand column of Fig. 3 shows the mass of the star+disc system and important disc properties, including mass, radius, specific angular momentum, average magnetic field and plasma beta. The star+disc system forms at $t \approx 1.01 t_{\rm ff}$. For the hydrodynamic model, 97 per cent of the mass that was initially in the gas cloud resides in the star+disc system by $t = 1.21\,t_{\rm ff}$ and 32 per cent of that mass resides in the disc. When magnetic fields are included, angular momentum is efficiently transported outwards, so the specific angular momentum in the disc decreases as the initial magnetic field strength is increased. As the initial magnetic field strength is increased, the disc radius and the masses of the disc and star+disc system decrease. For $\mu_0 = 5$, the majority of the high-density material is converted into the sink particle during its formation, and the remaining high-density material is quickly accreted; by $t \approx 1.08\,t_{\rm ff}$, all evidence of the disc has been erased. The non-smooth evolution of the disc radii is caused by gravitational instabilities that trigger transient features in the disc, including spiral arms. These are also pronounced since the disc characteristics are typically calculated at intervals of $\mathrm{d}t = 0.01\,t_{\rm ff}$.

This analysis is similar to the results in fig. 4 of PB07. While the same trends are observed, the quantitative results are different. This is a result of an error in the initial conditions of PB07, where the sound speed was not defined in the low-density background. This resulted in a slower collapse, and less gas reaching $\rho > \rho_{\rm disc,\,min}$ since the gas in the initial cloud was not pressure confined. Hence, they reported lower disc masses and radii. We were able to reproduce their values by simulating a model where our gas cloud was not in a pressure confined medium.

The relationship between magnetic field strength and density in these models is not as well defined as in Sections 2.2 and 2.3, where we described the ionization and conductivities; there, the magnetic field was defined as in (34). In these models, the relationship is typically $B \propto \rho^p$, where $p \in [\frac{1}{2}, \frac{2}{3}]$. This agrees with the range presented in Tsukamoto et al. (2015a). For the three magnetic models, the average magnetic field in the disc is similar; recall, though, that the these models had initial magnetic field strengths that differed only by a factor of 2.

In summary, hydrodynamical collapses result in large, massive discs while magnetohydrodynamical collapses hinder or suppress the formation of discs, with smaller discs forming in simulations with stronger initial magnetic fields – assuming a disc forms at all. In agreement with (e.g.) Allen et al. (2003), PB07, Mellon & Li (2008) and Hennebelle & Fromang (2008), this demonstrates the magnetic braking catastrophe.

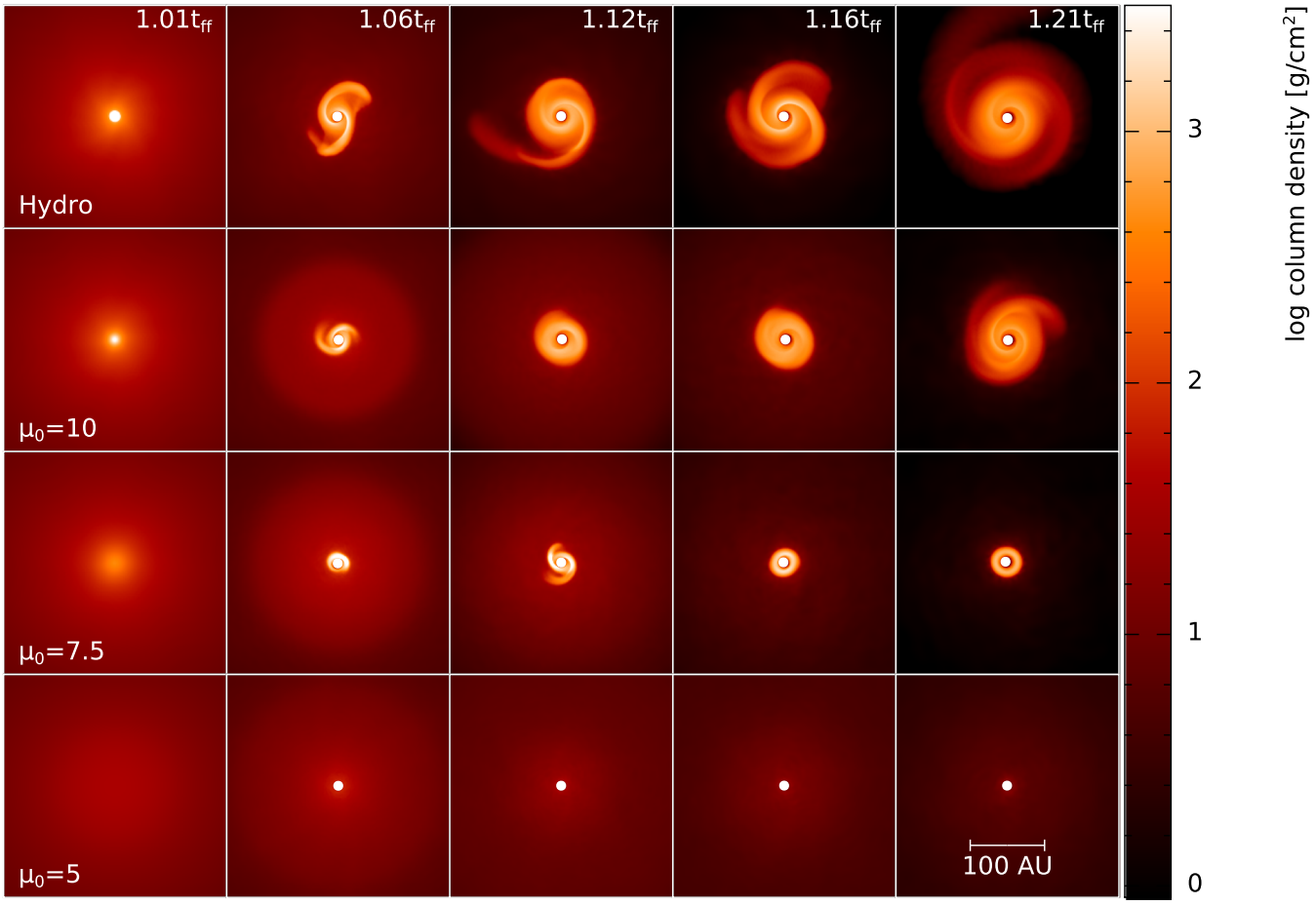

Figure 2. Face-on gas column density using ideal MHD. The initial rotation is counterclockwise and the initial magnetic field is directed out of the page (i.e. $\boldsymbol{B}_0 \cdot \boldsymbol{\Omega}_0 > 0$). Each model is initialized with $\sim 3 \times 10^5$ particles within the sphere. From left to right, the columns represent snapshots at a given time (in units of the free-fall time, $t_{\rm ff} = 2.4 \times 10^4$ yr). The rows represent models with different initial magnetic field strengths given in terms of μ_0 (i.e. the initial mass-to-flux ratio normalized to the critical mass-to-flux ratio). The top row has no initial magnetic field and the bottom row has the strongest magnetic field (i.e. increasing magnetic field strength corresponds to a decreasing value of μ_0). The white circles represent the sink particle with the radius of the circle representing the accretion radius of the sink particle. Each frame is $(300\ {\rm au})^2$. The discs grow in size and mass with time. At any given time, the models with stronger magnetic fields have smaller and less massive discs than the models with the weaker initial magnetic field. The hydrodynamic model yields the largest and most massive disc in our entire suite of simulations.

4.1.1 Resolution

Fig. 4 shows a comparison of the discs formed at resolutions of $\sim 3 \times 10^5$ particles in the collapsing sphere (top row) and $\sim 10^6$ particles (bottom row) using $\mu_0 = 7.5$. This magnetic field strength was used so that disc characteristics could be compared. The $\sim 10^6$ particle model took $\sim$3.5 times longer to run, which is reasonable given the increase in resolution.

The two resolutions follow the same general trend, with large discs forming. For $1.10 \lesssim t/t_{\rm ff}\tilde{} \lesssim \tilde{}1.21$, the star+disc mass, disc mass and disc radius typically differ by less than 20 per cent. Thus, these results are relatively robust to the resolution increase presented here.

4.2 Ideal MHD – outflows

Fig. 5 shows the edge-on column density for the ideal MHD calculations. We see that the models with magnetic fields launch bipolar outflows shortly after the collapse of the core, in agreement with Tomisaka (1998, 2002), Tomisaka, Machida & Matsumoto (2004), Machida, Tomisaka & Matsumoto (2004), Machida et al. (2006, 2008b), Hennebelle & Fromang (2008), Commerçon et al. (2010), Bürzle et al. (2011) and Price et al. (2012); stronger and more collimated outflows are launched in models with stronger magnetic fields. Some numerical asymmetries are visible at $t \gtrsim 1.12\, t_{\rm ff}$ in the $\mu_0 = 10$ and 7.5 models, which are caused by a lack of momentum conservation in the second term of (36). Angular momentum, however, is conserved within 2 per cent until sink formation. We have verified that the loss in conservation is independent of whether or not a sink particle is inserted. We also find that in ideal MHD, in agreement with previous authors, the outflow properties are resolution dependent. Hence, while a qualitative study of the outflows is useful, we urge caution regarding any quantitative properties.

4.3 Non-ideal MHD

Fig. 6 shows the face-on column density plots for three non-ideal MHD models using initial magnetic field strengths of $\mu_0 = 10$, 7.5 and 5; this figure is directly comparable to the bottom three rows in Fig. 2. Since the sign of $\boldsymbol{B}_0 \cdot \boldsymbol{\Omega}_0$ is important for the Hall effect, the top and bottom panels have the magnetic field initialized with $\boldsymbol{B}_0 \cdot \boldsymbol{\Omega}_0 > 0$ and <0, respectively.

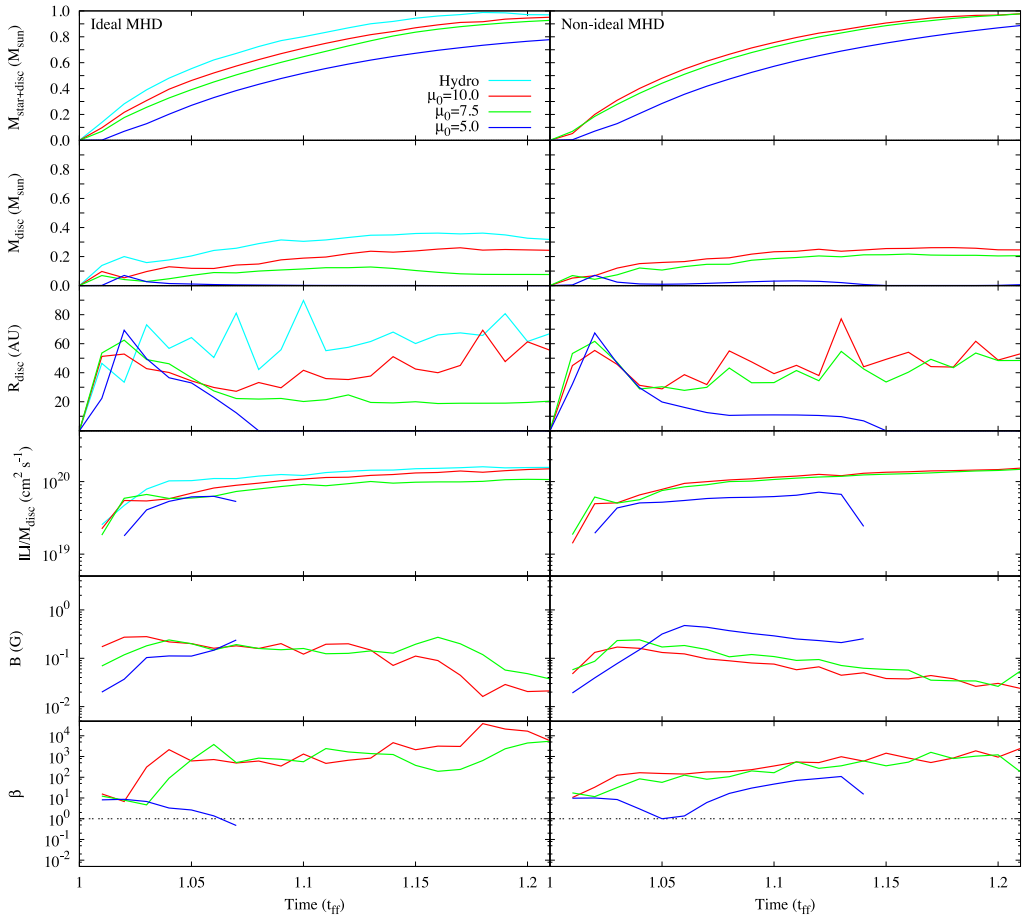

Figure 3. Disc properties for the ideal (left) and non-ideal (right) MHD models with $\sim 3 \times 10^5$ particles in the sphere. Top to bottom: mass of the star+disc system, the disc mass, disc radius, the specific angular momentum of the disc, the average magnetic field and the average plasma beta (this frame includes a reference line at $\beta = 1$, where gas and magnetic pressure are equal). The disc is defined by $\rho > \rho_{\rm disc,\,min} = 10^{-13}$ g cm^{-3}, which is one order of magnitude above which the gas becomes adiabatic. The disc radius is defined as the radius which contains 99 per cent of the mass of the star+disc system. The average magnetic field and plasma beta are averages over all of the particles in the disc. The masses of the disc and star+disc system, as well as the disc radius and specific angular momentum, decrease for increasing magnetic field strength. The hydrodynamic model yields the largest and most massive disc. Magnetic fields counteract the gravitational collapse, thus, for both ideal and non-ideal MHD, stronger magnetic fields yield smaller and less massive discs. For the models with $\mu_0 = 5$, all traces of the disc have been erased by $t \approx 1.08\,t_{\rm ff}$ and $\approx 1.15\,t_{\rm ff}$ for the ideal and non-ideal MHD models, respectively.

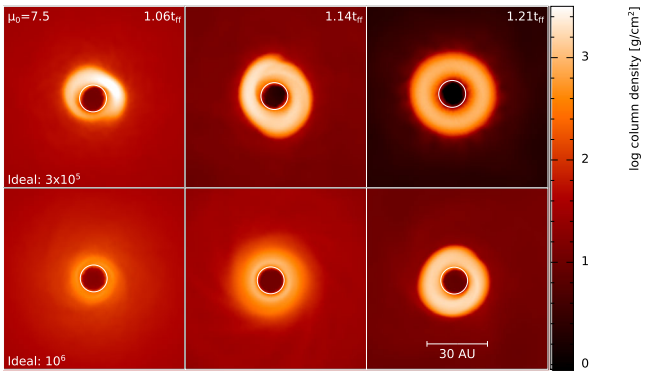

Figure 4. Face-on column density as in Fig. 2 but for ideal MHD at two different resolutions and zoomed in to (90 au)^2; both use $\mu_0 = 7.5$. The open circles represent the sink particle with the radius of the circle representing the accretion radius of the sink particle. At both resolutions, disc masses and radii are similar.

Of the $\boldsymbol{B}_0 \cdot \boldsymbol{\Omega}_0 > 0$ models, only the $\mu_0 = 10$ model forms a disc. At $t = 1.21\,t_{\rm ff}$, the non-ideal MHD model has a star+disc mass that is 4.2 per cent more massive and a disc that is 10 per cent less massive than its ideal MHD counterpart. The radii of the two discs differ by less than 30 per cent; at any given time throughout the evolution, there is up to 60 per cent difference in radius, although it varies which model has the larger disc.

Discs form in all three $\boldsymbol{B}_0 \cdot \boldsymbol{\Omega}_0 < 0$ models, and their characteristics are plotted in the right-hand column of Fig. 3. As with the ideal MHD models, increasing the initial magnetic field strength decreases the star+disc and disc masses and the radius of the disc, although the effect is not as pronounced as in the ideal MHD suite. Since a disc does not form in the ideal MHD model with $\mu_0 = 5$, it is reasonable to only compare star+disc masses. At the remaining two magnetic field strengths, the non-ideal MHD models have larger disc masses and radii, and the specific angular momentum is similar or slightly larger. The ideal MHD models have stronger magnetic fields in the disc; this is expected given the inclusion of the two dissipative terms in the non-ideal MHD models. On average, gas pressure dominates the magnetic pressure in the disc.

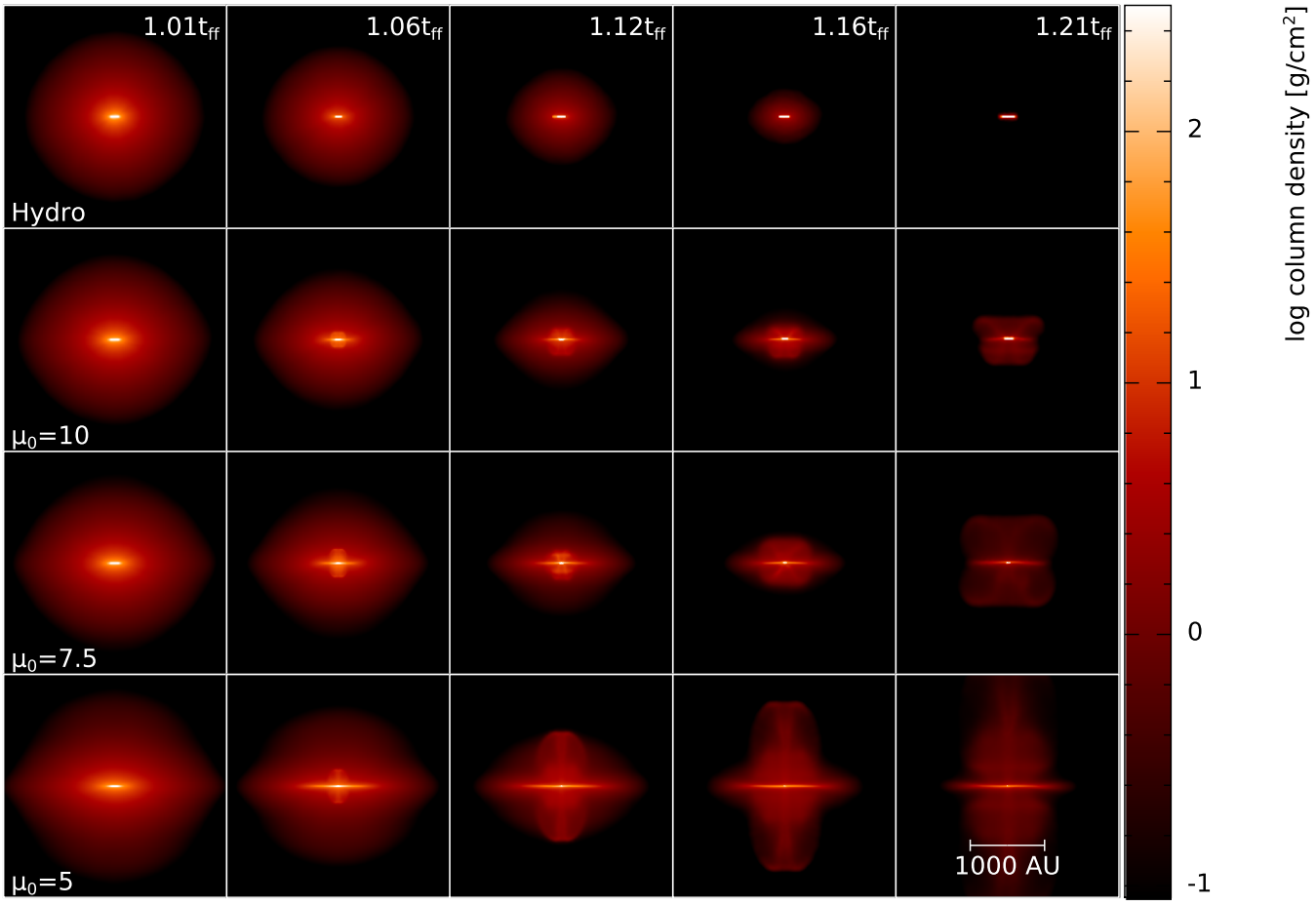

Figure 5. Edge-on gas column density using ideal MHD and zoomed out to $(3000\ \mathrm{au})^2$ and using a density range shifted down by a factor of 10 to visualize the full extent of the outflows launched shortly after the collapse ($t \approx 1.02\,t_{\rm ff}$) in the magnetic models. The models with stronger magnetic fields have faster and more collimated outflows.

4.3.1 Resolution

As with our ideal MHD simulations, we analyse the effect of increasing the resolution from $\sim 3 \times 10^5$ particles in the initial gas cloud to $\sim 10^6$ particles. Given the h^2 dependence that the smoothing length has on the non-ideal MHD timestep, the increase in runtime is considerable for the models that form discs and include the Hall effect (since super timestepping cannot be used). It takes the non-ideal MHD model with $\mu_0 = 5$, $\boldsymbol{B}_0 \cdot \boldsymbol{\Omega}_0 < 0$ and $\sim 10^6$ particles ~ 19 times longer to reach $t = 1.15\,t_{\rm ff}$ than its $\sim 3 \times 10^5$ particle counterpart; this is the time when the disc dissipates in the $\sim 3 \times 10^5$ model. For comparison, it takes the $\boldsymbol{B}_0 \cdot \boldsymbol{\Omega}_0 < 0$ model with $\sim 10^6$ particles ~ 6.8 times longer to reach $t = 1.21\,t_{\rm ff}$ than its $\sim 3 \times 10^5$ counterpart.

Fig. 7 shows the face-on gas column densities for the non-ideal MHD model with $\mu_0 = 5$ and $\boldsymbol{B}_0 \cdot \boldsymbol{\Omega}_0 < 0$, and Fig. 8 shows the disc characteristics. Increasing the resolution for the non-ideal MHD models has a minimal effect on the disc over the time of analysis ($t \leq 1.15\,t_{\rm ff}$; i.e. the life of the disc in the $\sim 3 \times 10^5$ model). By increasing the resolution, the mass of the star+disc system decreases only by ~ 5 per cent. The high-resolution disc is more massive within a factor of 2 than its counterpart, and the evolution indicates that it will not dissipate.

Our $\sim 3 \times 10^5$ particle models meet the resolution criteria set out by Bate & Burkert (1997, cf. Section 3), and our brief resolution study indicates that our results agree at both resolutions. Thus, to save computational costs of the $\boldsymbol{B}_0 \cdot \boldsymbol{\Omega}_0 < 0$ models with weaker magnetic fields, the bottom panel in Fig. 6 shows the lower resolution models. For consistency, we thus present all the models in Sections 4.1 and 4.3 at the lower resolution. The remainder of this study is performed using the $\sim 10^6$ particle models, with the exception of our discussion of the cosmic ionization rate. Note that the non-ideal MHD model with $\mu_0 = 5$ and $\boldsymbol{B}_0 \cdot \boldsymbol{\Omega}_0 < 0$ has only evolved to $t \approx 1.18\,t_{\rm ff}$.

4.4 Non-ideal MHD – outflows

Fig. 9 shows the edge-on column density for the non-ideal MHD calculations, showing the models with $\boldsymbol{B}_0 \cdot \boldsymbol{\Omega}_0 > 0$ and $\boldsymbol{B}_0 \cdot \boldsymbol{\Omega}_0 < 0$ in the top and bottom plots, respectively. The most interesting aspect is that outflows appear to anticorrelate with the presence of discs. That is, outflows carry away angular momentum, which hinders the formation of discs. This is counterintuitive since one would normally expect outflows to be launched from a disc. Here, as in Price et al. (2012), the outflows are powered by a rotating, sub-Keplerian flow, and carry away sufficient angular momentum to prevent the formation of a Keplerian disc. Non-ideal MHD, in general, appears to suppress the formation of outflows. This is quantified further in Section 4.6, where we discuss the influence of individual non-ideal MHD terms.

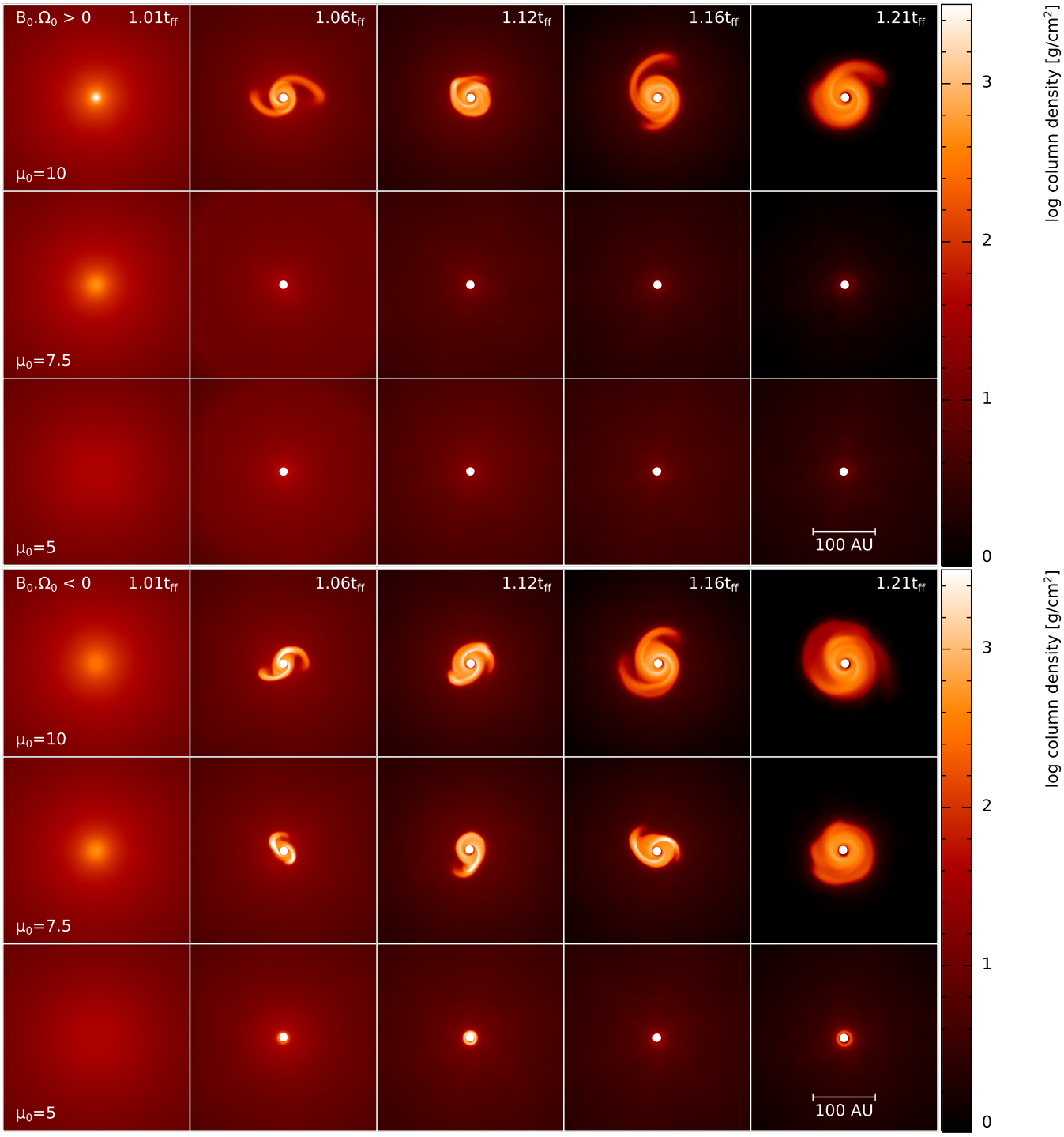

Figure 6. Face-on gas column density, as in Fig. 2 but for non-ideal MHD including the effect of Ohmic resistivity, the Hall effect and ambipolar diffusion. The top plot has the magnetic field initialized with $\boldsymbol{B}_0 \cdot \boldsymbol{\Omega}_0 > 0$, and the bottom plot with $\boldsymbol{B}_0 \cdot \boldsymbol{\Omega}_0 < 0$. Compared to ideal MHD, disc sizes are smaller for $\boldsymbol{B}_0 \cdot \boldsymbol{\Omega}_0 > 0$, but larger for $\boldsymbol{B}_0 \cdot \boldsymbol{\Omega}_0 < 0$. This indicates that the Hall effect is the most important non-ideal MHD term for disc formation.

4.5 Which non-ideal MHD terms are important?

The results in Section 4.3 clearly show the importance of including non-ideal MHD. To determine the specific effect of each term, we model the collapse using only one non-ideal MHD term at a time, and using both signs of $\boldsymbol{B}_0 \cdot \boldsymbol{\Omega}_0$ in models that include the Hall effect. These models represent contrived and idealized situations since the physical environment dictates the importance of each term, thus these terms cannot be selected a priori. However, these models will allow us to determine the impact each effect has, as well as to compare our results to those in the literature. Figs 10 and 11 show the face-on and edge-on gas column density, respectively, for the ideal MHD, Ohmic-only, Hall-only (for $\boldsymbol{B}_0 \cdot \boldsymbol{\Omega}_0 > 0$ and <0), ambipolar-only and non-ideal MHD (for $\boldsymbol{B}_0 \cdot \boldsymbol{\Omega}_0 > 0$ and <0) models. All simulations use $\sim 10^6$ particles in the sphere and

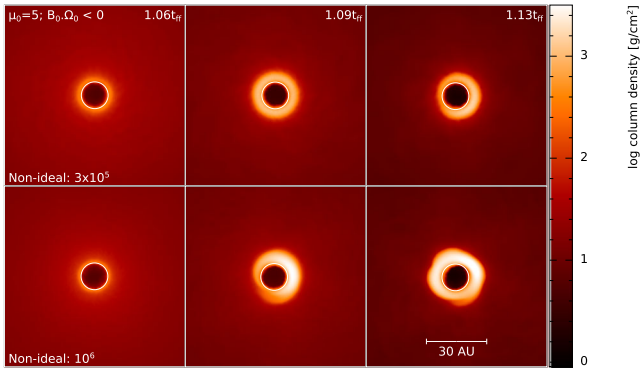

Figure 7. Resolution study, as in Fig. 4, but for non-ideal MHD with $\mu_0 = 5$ and $\boldsymbol{B}_0 \cdot \boldsymbol{\Omega}_0 < 0$. For non-ideal MHD, increasing the resolution decreases the mass of the star+disc system by only ∼5 per cent.

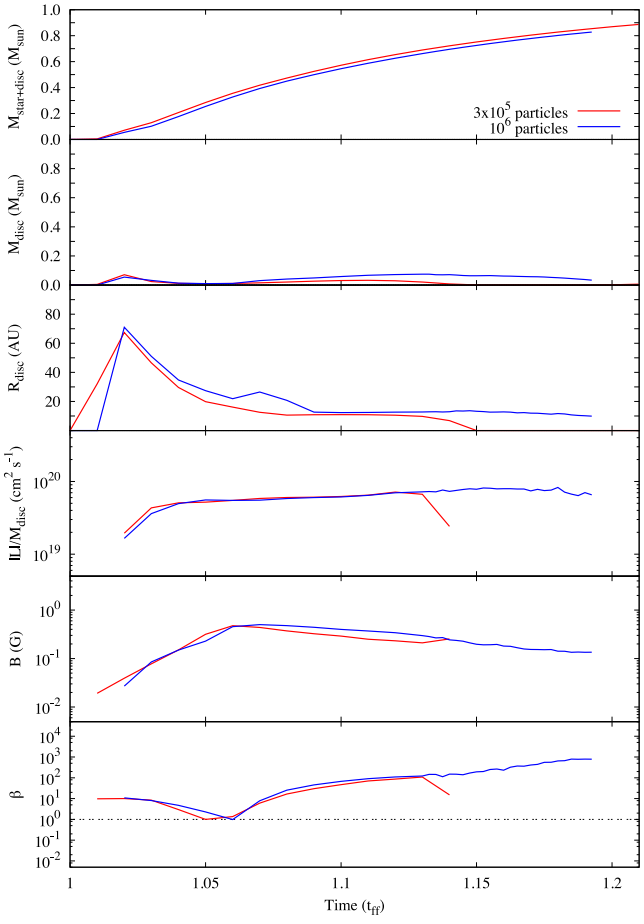

Figure 8. As in Fig. 3 but for the non-ideal MHD models with $\boldsymbol{B}_0 \cdot \boldsymbol{\Omega}_0 < 0$ and $\mu_0 = 5$ at resolutions of $\sim 3 \times 10^5$ and $\sim 10^6$ particles in the sphere. At $t = 1.15\,t_{\rm ff}$, the star+disc system masses differ by less than ∼5 per cent. The $\sim 10^6$ model has only evolved to $t \approx 1.18\,t_{\rm ff}$.

$\mu_0 = 5$, since this is the magnetic field strength in our suite that it is most comparable to observed magnetic field strengths

At this resolution and magnetic field strength, discs form in the ideal MHD and Ohmic-only models at $t \approx 1.17\,t_{\rm ff}$; by $t = 1.21\,t_{\rm ff}$, these discs have grown to $r \approx 14$ and 13 au, respectively. The ambipolar-only model, and the models that include the Hall effect with $\boldsymbol{B}_0 \cdot \boldsymbol{\Omega}_0 > 0$ fail to form discs. Large discs are formed when the Hall effect is included and the gas is initialized with $\boldsymbol{B}_0 \cdot \boldsymbol{\Omega}_0 < 0$.

Qualitatively, the Hall effect with $\boldsymbol{B}_0 \cdot \boldsymbol{\Omega}_0 < 0$ appears to be the most important non-ideal MHD term. Quantitatively, the importance of each non-ideal term in the disc can be analysed using the non-ideal MHD model with $\boldsymbol{B}_0 \cdot \boldsymbol{\Omega}_0 < 0$. The left-hand panel of Fig. 12 shows the average coefficients of the three non-ideal MHD terms and the artificial resistivity, η, and magnetic Reynolds number, $R_{\rm m}$, in the disc at any given time; the right-hand panel shows the radial profile of these terms at $t = 1.12\,t_{\rm ff}$.

Shortly after the formation of the disc, the Hall effect is the dominant term, and ambipolar diffusion is comparable to the artificial resistivity. As the system evolves, ambipolar diffusion becomes the dominant term, and the Hall effect becomes less important. Ohmic resistivity becomes important as the density of the disc increases. At the snapshot of $t = 1.12\,t_{\rm ff}$, ambipolar diffusion and Ohmic resistivity dominate the Hall effect within the defined disc. When considering earlier times (e.g. $1.06\,t_{\rm ff}$), the radial profile is approximately constant with radius, with $|\bar{\eta}_{\rm HE}| > \bar{\eta}_{\rm art} > \bar{\eta}_{\rm AD} > \bar{\eta}_{\rm OR}$.

A magnetic Reynolds number, $R_{\rm m} = v_{\rm C} r/\eta$, where $v_{\rm C} = \sqrt{GM(r)/r}$ is the circular velocity at radius r and $M(r)$ is the enclosed star+disc mass, is calculated for each physical and artificial resistivity. For all time, at least one Reynolds number from a physical terms is lower than the Reynolds number from artificial resistivity. This indicates that the physical resistivity is more important than artificial resistivity. Moreover, the value of $R_{\rm m} \gtrsim 1$ indicates that the diffusion terms are important in the disc.

4.6 Effect of non-ideal MHD terms – outflows

All models that include magnetic fields launch bipolar outflows. Increasing the magnetic field strength (i.e. Sections 4.1 and 4.3) yields faster and more collimated outflows, which are sustained over a longer period of time.

At $\mu_0 = 5$ (cf. Figs 10 and 11), both the ideal MHD and Ohmic-only models launch strong, collimated outflows. As the systems evolve, the base of the outflow broadens, resulting in a less collimated system, although the remnant of the collimated outflow persists. By the time the disc forms at $t \approx 1.17\,t_{\rm ff}$, the outflow has been well established and is in the process of weakening. When the Hall effect or ambipolar diffusion are included for $\boldsymbol{B}_0 \cdot \boldsymbol{\Omega}_0 > 0$, broad outflows form; unlike the ideal MHD and Ohmic-only models, there is no collimated central outflow. Thus, in models that do not form discs, strong bipolar outflows form, and the Hall effect and ambipolar diffusion prevent collimation.

A large disc forms in the Hall-only model with $\boldsymbol{B}_0 \cdot \boldsymbol{\Omega}_0 < 0$, however the outflow is almost completely suppressed. A weak outflow is launched at $t \approx 1.05\,t_{\rm ff}$, but dissipates by $\approx 1.08\,t_{\rm ff}$. A small dense disc forms in the non-ideal MHD model with $\boldsymbol{B}_0 \cdot \boldsymbol{\Omega}_0 < 0$, and a weak outflow is launch at $t \approx 1.07\,t_{\rm ff}$. The outflow continues to expand as the system evolves, however it is never collimated and never becomes as broad as in the $\boldsymbol{B}_0 \cdot \boldsymbol{\Omega}_0 > 0$ models.

As discussed in Section 4.4, we find that the presence of a collimated outflow is anticorrelated to the presence of a large disc.

4.7 Effect of magnetic field direction

The direction of the magnetic field with respect to the rotation vector (i.e. the sign of $\boldsymbol{B}_0 \cdot \boldsymbol{\Omega}_0$) has a profound impact. This can be seen by comparing third to the fourth row (Hall-only), and the seventh to the eighth row (non-ideal MHD) of Figs 10 and 11; the bottom row in each pair is initialized with $\boldsymbol{B}_0 \cdot \boldsymbol{\Omega}_0 < 0$. Using $\boldsymbol{B}_0 \cdot \boldsymbol{\Omega}_0 < 0$, an $r \approx 38$ au disc forms in the Hall-only model, and an $r \approx 13$ au disc forms in the non-ideal MHD model by $t = 1.15\,t_{\rm ff}$; the Hall-only

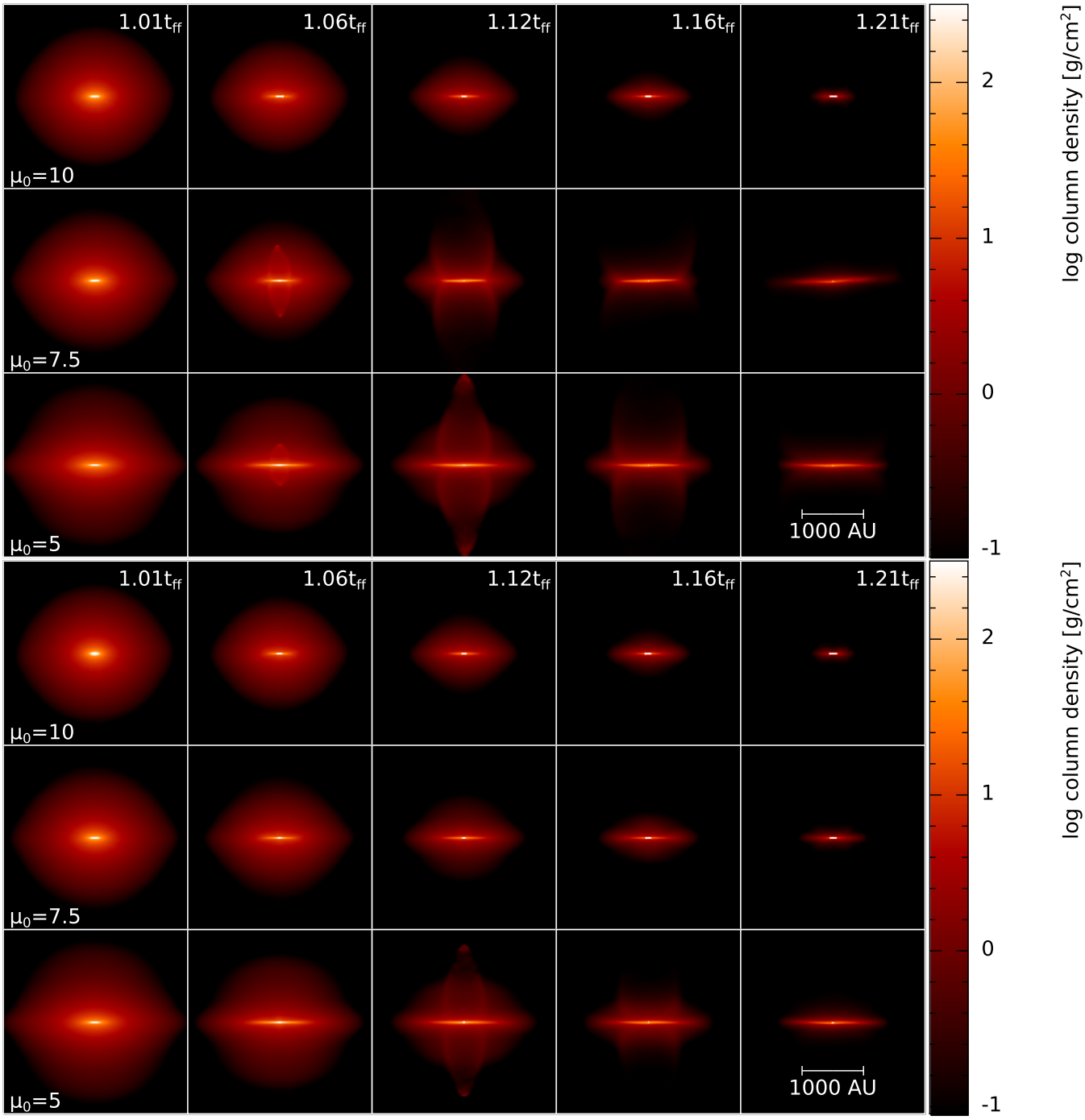

Figure 9. Edge-on gas column density, as in Fig. 5 but for non-ideal MHD including the effect of Ohmic resistivity, the Hall effect and ambipolar diffusion. The top plot has the magnetic field initialized with $\boldsymbol{B}_0 \cdot \boldsymbol{\Omega}_0 > 0$, and the bottom plot with $\boldsymbol{B}_0 \cdot \boldsymbol{\Omega}_0 < 0$. Outflows form in the calculations that form small discs.

model has its maximum disc radius at this time. Thus, at a magnetic field strength of $\mu_0 = 5$, discs can only be formed if the Hall effect is included and $\boldsymbol{B}_0 \cdot \boldsymbol{\Omega}_0 < 0$.

Fig. 13 shows the masses and sizes of these discs (along with the limited information from their $\boldsymbol{B}_0 \cdot \boldsymbol{\Omega}_0 > 0$ counterparts). In all five models in this figure, a sink particle is formed at $t \approx 1.025\, t_{\rm ff}$. By $t \approx 1.07\, t_{\rm ff}$, the disc disappears in the Hall-only and non-ideal MHD models with $\boldsymbol{B}_0 \cdot \boldsymbol{\Omega}_0 > 0$ as the remainder of the high-density ($\rho > \rho_{\rm disc,\,min}$) material is accreted on to the sink particle. In these models, a true 'disc' may never have formed, and the reported disc properties are for the high-density material that satisfies our chosen definition of 'disc'. Thus, at this magnetic field strength, there are no discs with $\boldsymbol{B}_0 \cdot \boldsymbol{\Omega}_0 > 0$ to which we can compare.

The star+disc masses in the $\boldsymbol{B}_0 \cdot \boldsymbol{\Omega}_0 < 0$ models are ∼23 and 9 per cent more massive than their $\boldsymbol{B}_0 \cdot \boldsymbol{\Omega}_0 > 0$ counterparts for the Hall-only and non-ideal MHD models, respectively, at $t = 1.15\, t_{\rm ff}$. At $t = 1.21\, t_{\rm ff}$, the Hall-only model with $\boldsymbol{B}_0 \cdot \boldsymbol{\Omega}_0 < 0$ has a large disc, which is ∼64 and ∼68 per cent smaller in mass and radius, respectively, than the hydrodynamic disc.

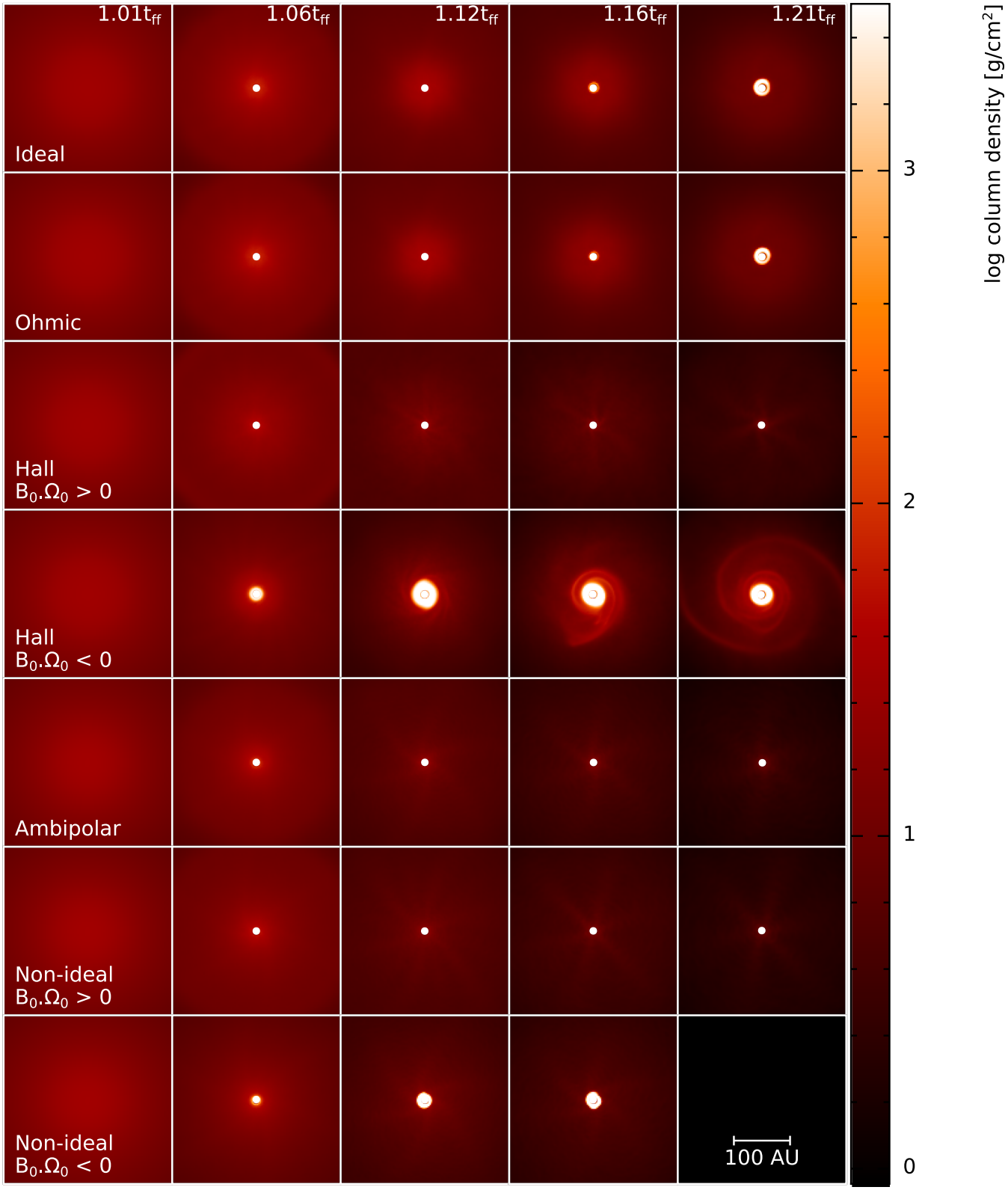

Figure 10. As in Fig. 2 but for ideal MHD, Ohmic-only, Hall-only, ambipolar-only and non-ideal MHD models, using $\mu_0 = 5$ and $\sim 10^6$ particles in the sphere. The Hall effect is sensitive to the sign of $\boldsymbol{B}_0 \cdot \boldsymbol{\Omega}_0$, thus models including the Hall effect are modelled using both orientations of the initial magnetic field; all other models are insensitive to the sign of $\boldsymbol{B}_0 \cdot \boldsymbol{\Omega}_0$ thus use $\boldsymbol{B}_0 \cdot \boldsymbol{\Omega}_0 > 0$. Small discs form at late times in the ideal MHD and Ohmic-only models. In the Hall-only and non-ideal MHD models, $r \approx 38$ and 13 au disc exists by $t = 1.15\, t_{\rm ff}$, respectively. The non-ideal MHD model with $\mu_0 = 5$ and $\boldsymbol{B}_0 \cdot \boldsymbol{\Omega}_0 < 0$ has only evolved to $t \approx 1.18\, t_{\rm ff}$.

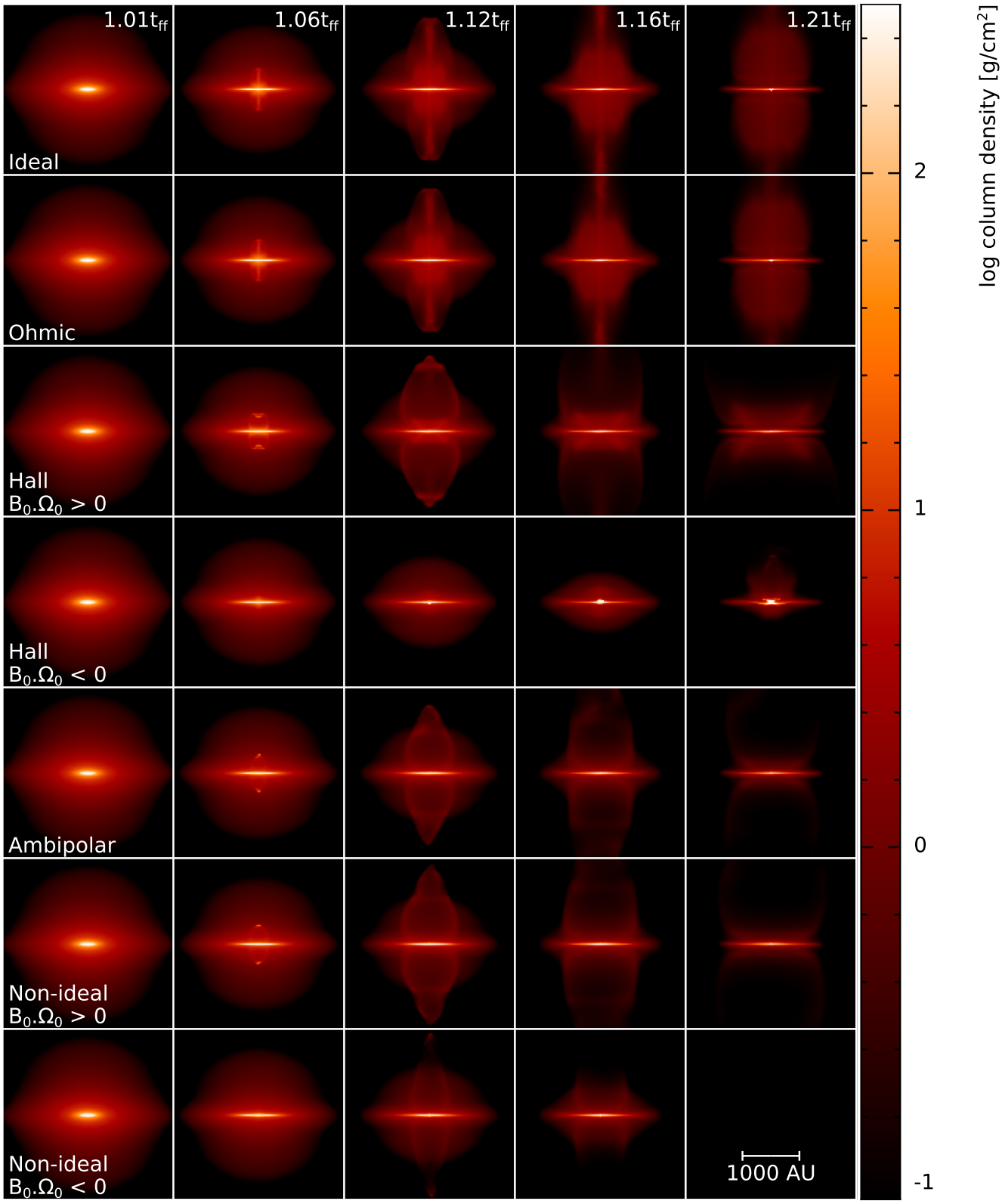

Figure 11. As in Fig. 10 but showing the edge-on gas column density. Strong outflows correspond to models with small or no discs, and the outflow is more collimated for more ideal models (i.e. ideal MHD and Ohmic-only models).

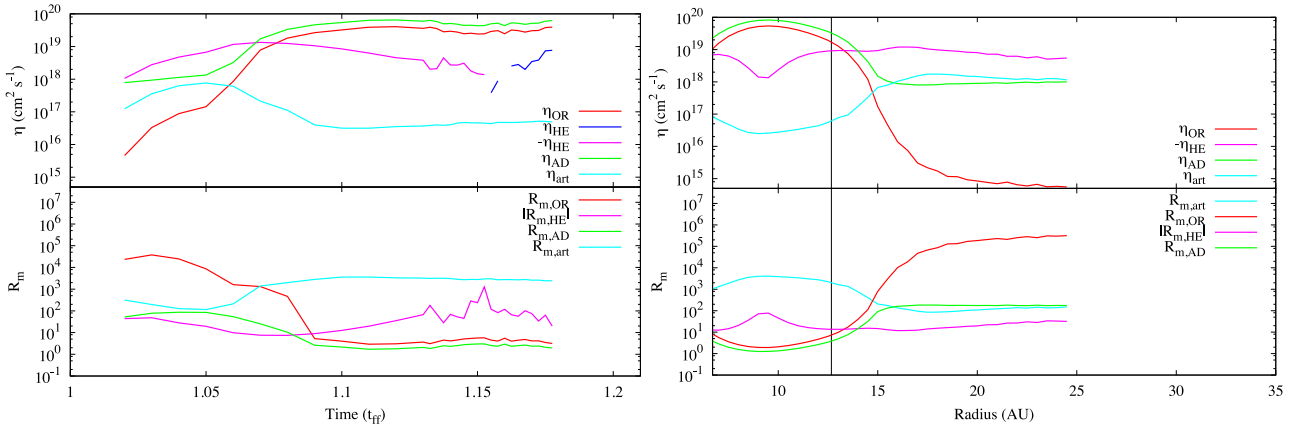

Figure 12. Non-ideal MHD coefficients, η (top panels) and magnetic Reynolds numbers, $R_\mathrm{m} = v_\mathrm{C} r/\eta$ (bottom panels) for the non-ideal MHD model with $\mu_0 = 5$ and $\boldsymbol{B}_0 \cdot \boldsymbol{\Omega}_0 < 0$. The left-hand panel shows the average values in the disc, and the right-hand panel shows the radial profile at $t = 1.12\,t_\mathrm{ff}$. Horizontal axes are chosen for consistency with other plots in this paper. The vertical line in the right-hand panel corresponds to the defined radius of the disc at that time. Shortly after the formation of the disc, the Hall effect is the dominant term, but as the disc begins to dissipate, the dissipative terms begin to dominate. The value of $R_\mathrm{m} \gtrsim 1$ indicates that the diffusion terms are important in the disc.

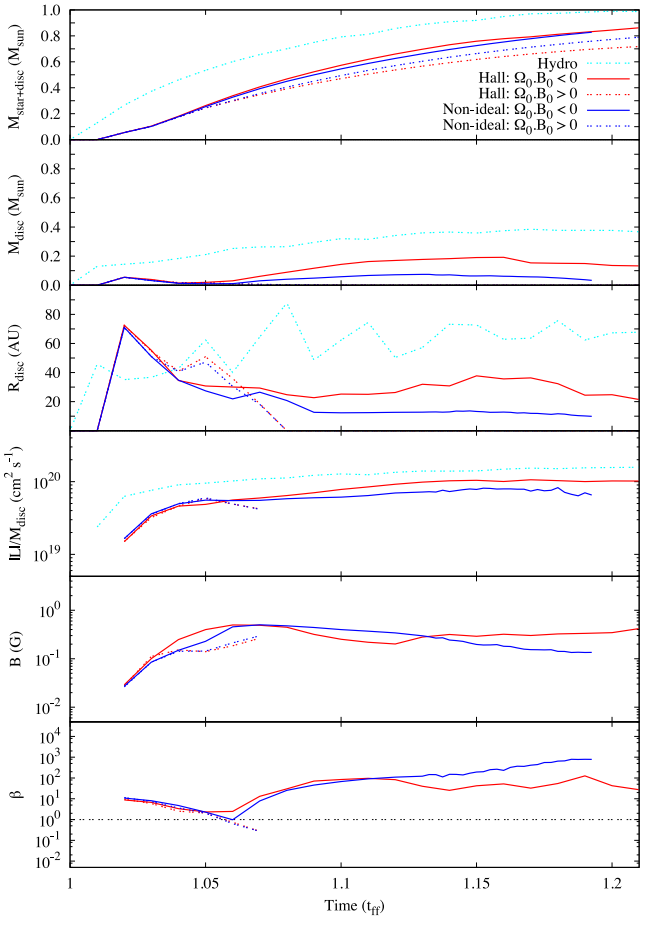

Figure 13. Disc properties as in Fig. 3, but for Hall-only (red) and non-ideal MHD (blue) models with $\boldsymbol{B}_0 \cdot \boldsymbol{\Omega}_0 < 0$ (solid lines) and $\boldsymbol{B}_0 \cdot \boldsymbol{\Omega}_0 > 0$ (dashed lines) for $\mu_0 = 5$ and $\sim 10^6$ particles. The properties for the hydrodynamical model are included for reference. In both cases, initializing the magnetic field such that $\boldsymbol{B}_0 \cdot \boldsymbol{\Omega}_0 < 0$ permits a disc to form, and yields a larger star+disc mass than their $\boldsymbol{B}_0 \cdot \boldsymbol{\Omega}_0 > 0$ counterpart. The non-ideal MHD model with $\mu_0 = 5$ and $\boldsymbol{B}_0 \cdot \boldsymbol{\Omega}_0 < 0$ has only evolved to $t \approx 1.18\,t_\mathrm{ff}$.

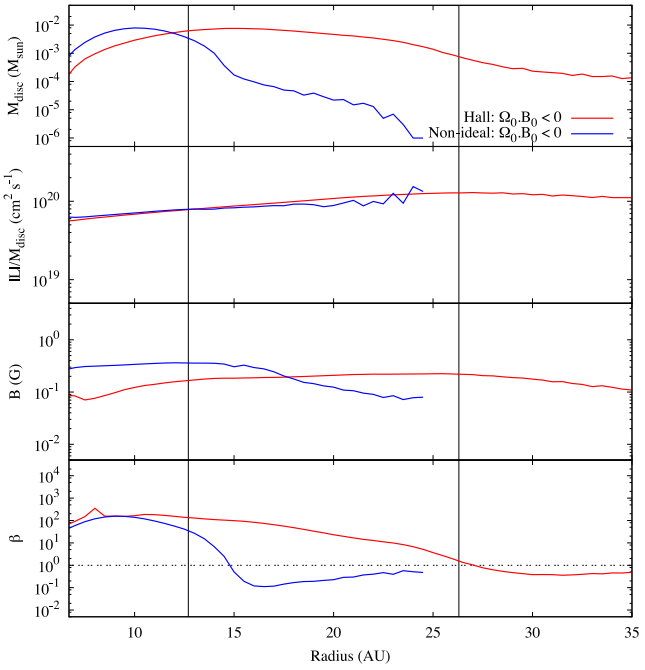

Figure 14. Radial profile of the disc at $t = 1.12\,t_\mathrm{ff}$ for the Hall-only (red) and non-ideal MHD (blue) models with $\boldsymbol{B}_0 \cdot \boldsymbol{\Omega}_0 < 0$, for $\mu_0 = 5$ and $\sim 10^6$ particles. The profile includes all the gas particles with density $\rho > \rho_{\mathrm{disc,\,min}}$, and starts at $r = 6.7$ au, which is the sink radius. The vertical lines at $\sim$13 and 26 au represent the defined radii of the discs in the non-ideal MHD and Hall-only models, respectively. From top to bottom: disc mass, specific angular momentum, magnetic field strength and plasma beta.

Both $\boldsymbol{B}_0 \cdot \boldsymbol{\Omega}_0 < 0$ models have magnetic field strengths and plasma beta's that differ by less than a factor of 2. Thus, the Hall effect is the non-ideal MHD term that is primarily responsible for preventing the transport of angular momentum to allow the disc to grow.

Although average trends appear similar between both models, the radial structure of both discs differs, as shown in Fig. 14 at a snapshot at $t = 1.12\,t_\mathrm{ff}$. When considering the magnetic field profile, the Hall-only model has a maximal magnetic field strength at $r \approx$ 26 au, which does not correspond to the radius of the maximum

mass. Thus, the Hall effect traps the magnetic field at a larger radius, which is near the outer edge of the disc. Interior to this, and ignoring the slight rise in magnetic field strength near the sink particle, the maximum plasma beta of $\beta \approx 184$ is at $r \approx 11$ au, corresponding to a weaker magnetic field.

When all three non-ideal MHD terms are present, the dissipative processes diffuse the magnetic field, and the maximum field strength is reduced. However, these processes also diffuse the field inwards, so the magnetic field for the non-ideal MHD model is stronger than the Hall-only model for the inner $r \approx 18$ au. Unlike the Hall-only model, the maximum mass and plasma beta occurs in the non-ideal MHD model at $r \approx 9$ au; this radius also corresponds to the maximum non-ideal coefficients, η (cf. the left-hand panel of Fig. 12). Within the defined disc, the magnetic field strength differs by less than 7 per cent, but the magnetic pressure is less important with respect to the gas pressure.

The previous analysis has focused on the formation of the disc, however, the surrounding gas is also affected by the processes and parameters, as suggested by Fig. 11. Fig. 15 shows the velocity perpendicular to a slice through the outflow (i.e. v_y) at $t = 1.12\,t_{\rm ff}$ for the ideal MHD model, and the Hall-only and non-ideal MHD models for both $\boldsymbol{B}_0 \cdot \boldsymbol{\Omega}_0 > 0$ and <0. In all models, the gas is initially rotating counterclockwise, and in the $\boldsymbol{B}_0 \cdot \boldsymbol{\Omega}_0 > 0$ models, it continues to do so as the system evolves. The velocity structure of the ideal MHD model traces the established collimated outflow and the young broad outflow (cf. Fig. 11). The Hall-only and non-ideal MHD models with $\boldsymbol{B}_0 \cdot \boldsymbol{\Omega}_0 > 0$ have a large opening angle, which corresponds to the broad outflow.

When the Hall effect is included in the $\boldsymbol{B}_0 \cdot \boldsymbol{\Omega}_0 < 0$ models, the large angular momentum in the disc results in a decrease in the angular momentum of the gas in the cloud from conservation laws, and causes a counter-rotating envelope to form. This can be clearly seen for the Hall-only model, where a counter-rotating envelope exists at a radius of $r \in (90, 150)$ au from the rotation axis. The non-disc material interior to this is slowly rotating, which is distinct from the remaining models. A weak counter-rotating envelope also exists in the non-ideal MHD models at $r \gtrsim 150$ au.

4.7.1 *Comparison to other works*

Given the numerical difficulty associated with the Hall effect, it has been previously ignored in disc collapse simulations, with the exception of Tsukamoto et al. (2015b), who independently performed similar collapse simulations while this study was being undertaken.

In the shearing box simulations of Bai (2014, 2015), their $\boldsymbol{B}_0 \cdot \boldsymbol{\Omega}_0 < 0$ models reduce the horizontal magnetic field which results in negligible magnetic braking. This would result in the formation of large discs, similar to the results obtained in our simulations.

Using self-similar calculations, Braiding & Wardle (2012a) concluded that the Hall effect is important in determining whether a disc forms, its size, density and rotational profiles. For $\boldsymbol{B}_0 \cdot \boldsymbol{\Omega}_0 > 0$, their solutions yield a decrease in surface density of the disc compared to a disc without the Hall effect. For $\boldsymbol{B}_0 \cdot \boldsymbol{\Omega}_0 < 0$, they determined that the surface density of the disc would be increased to realistic values for protostellar discs. They also show that a large amount of Hall diffusion is not required to create the asymmetry caused by the sign of $\boldsymbol{B}_0 \cdot \boldsymbol{\Omega}_0$ to be observable. While we were unable to control the strength of $\eta_{\rm Hall}$ since it is self-consistently calculated, we did achieve noticeable differences in the non-ideal MHD models even when the Hall effect had a secondary effect to ambipolar diffusion.

Similar to this study, Tsukamoto et al. (2015b) modelled the collapse of a uniform sphere of gas of $M = 1$ M$_\odot$ with

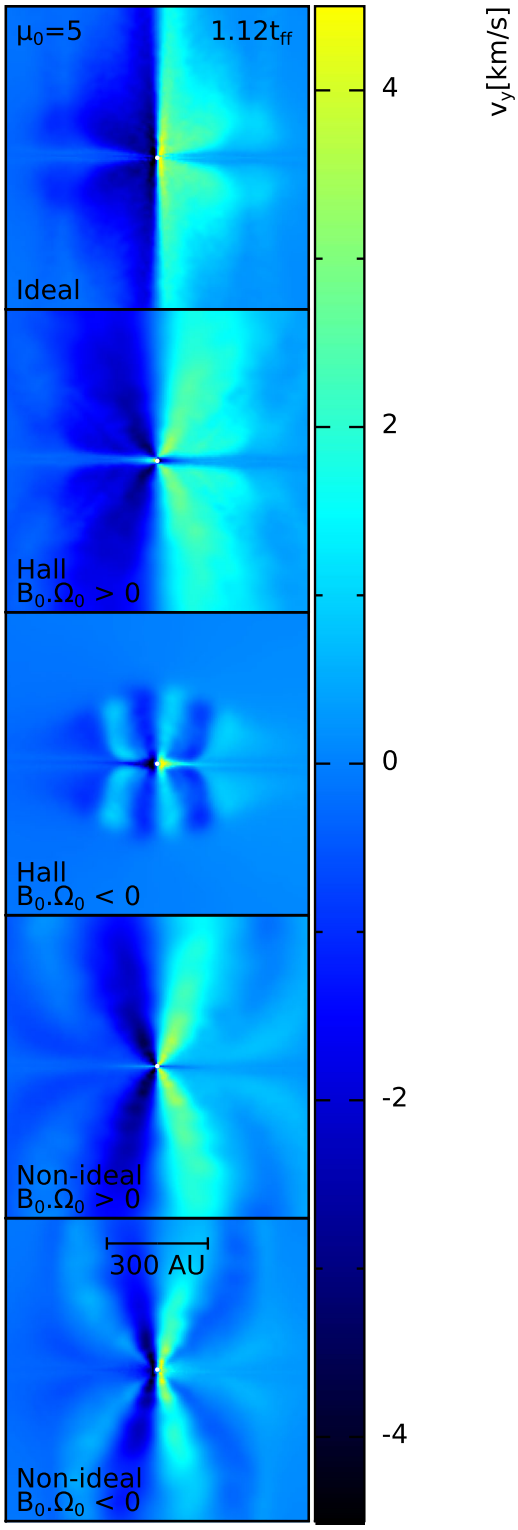

Figure 15. The velocity perpendicular to a slice through the outflow (i.e. v_y) for five models with $\mu_0 = 5$ at $t = 1.12\,t_{\rm ff}$. Each frame is (900 au)^2, which is smaller than in Fig. 11 so that details around the first hydrostatic core can be seen. The Hall-only model the $\boldsymbol{B}_0 \cdot \boldsymbol{\Omega}_0 < 0$ has a weak bipolar outflow, but forms a counter-rotating envelope. A weak counter-rotating envelope also exists in the non-ideal MHD model with $\boldsymbol{B}_0 \cdot \boldsymbol{\Omega}_0 < 0$. None of the other models develop a counter-rotating envelope. The Ohmic-only and ambipolar-only models are very similar to the ideal and non-ideal MHD ($\boldsymbol{B}_0 \cdot \boldsymbol{\Omega}_0 > 0$) models, respectively.

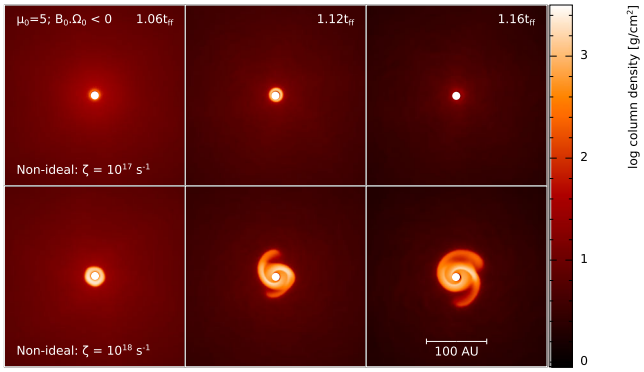

Figure 16. As in Fig. 2, but for two different cosmic ray ionization rates, ζ, for the non-ideal MHD model with $\mu_0 = 5$, $\boldsymbol{B}_0 \cdot \boldsymbol{\Omega}_0 < 0$, and $\sim 3 \times 10^5$ particles initially in the sphere. For this model, decreasing ζ allows a large disc to form and persist for the duration of the simulation; for the larger value of ζ, the disc dissipates by $t \approx 1.15\, t_{\rm ff}$.

$\mu_0 = 4$. These models included the Hall effect. When their cloud was initialized with $\boldsymbol{B}_0 \cdot \boldsymbol{\Omega}_0 > 0$, the result was a disc of $r < 1$ au, while for $\boldsymbol{B}_0 \cdot \boldsymbol{\Omega}_0 < 0$, the resulting disc had a radius of $r > 20$ au. This is consistent with our results, where our Hall-only models yielded no disc and an $r \approx 38$ au disc by $t = 1.15\, t_{\rm ff}$ for the two different orientations, respectively. Given our sink radius of $r = 6.7$ au, we are unable to resolve discs smaller than that; given our slightly weaker initial magnetic field, we expect a larger disc in our $\boldsymbol{B}_0 \cdot \boldsymbol{\Omega}_0 < 0$ model. Further, their Hall-only model with $\boldsymbol{B}_0 \cdot \boldsymbol{\Omega}_0 < 0$ forms a counter-rotating envelope similar in size and velocity as ours.

4.8 Effect of the cosmic ray ionization rate

As discussed in Section 2.2, the cosmic ray ionization rate, ζ, is one of the few free parameters in our algorithm. To test the effect of this parameter, we decrease it by a factor of 10 from our fiducial value of $\zeta = 10^{-17}$ s^{-1} to make the simulations 'more non-ideal.' This decrease in ζ causes a decrease in $\mathrm{d}t_{\rm non\text{-}ideal}$, and the runtime is substantially increased; the exact slow-down is model dependent. Given the slow-down in the models that form discs, the results in this section are complied from the $\sim 3 \times 10^5$ particle models.

In the non-ideal MHD model with $\boldsymbol{B}_0 \cdot \boldsymbol{\Omega}_0 > 0$, ζ has negligible effect, and neither model produces a disc. The model with $\zeta = 10^{-18}$ s^{-1} has a runtime $\sim$3.25 times longer than its fiducial-ζ counterpart.

For $\boldsymbol{B}_0 \cdot \boldsymbol{\Omega}_0 < 0$, a disc forms for both values of ζ. Fig. 16 shows the face-on column density for the non-ideal MHD models using $\zeta = 10^{-17}$ (top) and 10^{-18} s^{-1} (bottom); both models use $\mu_0 = 5$. Decreasing the value of ζ in this model increases the runtime by a factor of $\sim$30, and $\mathrm{d}t_{\rm Hall}$ is typically the limiting timestep after a free-fall time. The resulting disc is larger and more stable (i.e. survives for a longer period of time) for the $\zeta = 10^{-18}$ s^{-1} model. Fig. 17 shows the disc properties at a snapshot at $t = 1.12 t_{\rm ff}$. In both models, the magnetic field strength in approximately constant, but is $\sim$3 times higher in the $\zeta = 10^{-17}$ s^{-1} model. The maximum plasma beta is also $\sim$15 times higher in the $\zeta = 10^{-18}$ s^{-1} model, indicating weaker magnetic fields.

This analysis was intentionally performed using a model with the Hall effect and $\boldsymbol{B}_0 \cdot \boldsymbol{\Omega}_0 < 0$ since a disc forms. Tests show that the ambipolar-only model is insensitive to the value of the cosmic ionization rate. Thus, the physical differences are insensitive to the precise value of ζ, with the exception of models that include the Hall effect which are initialized with $\boldsymbol{B}_0 \cdot \boldsymbol{\Omega}_0 < 0$.

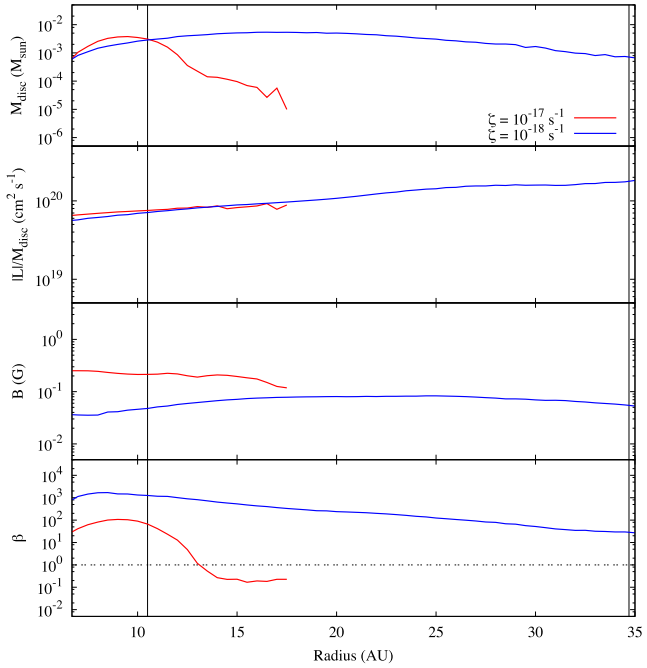

Figure 17. As in Fig. 14, but for two different cosmic ray ionization rates, ζ, for the non-ideal MHD model with $\mu_0 = 5$ and $\boldsymbol{B}_0 \cdot \boldsymbol{\Omega}_0 < 0$. The vertical lines at $r \approx 11$ and 35 au represent the defined radii of the discs using $\zeta = 10^{-17}$ and 10^{-18} s^{-1}, respectively.

4.9 Comparison to other works

The studies presented in previous works, such as Li et al. (2011), Tomida et al. (2015) and Tsukamoto et al. (2015a), are complementary to this study. Caution must be used, however, when comparing the studies to one another and to ours since there are differences in initial conditions, physical and numerical processes. None of these studies included the Hall effect. Regardless of the differences between the studies, a qualitative comparison is useful.

Li et al. (2011) ran a suite of 2D axisymmetric simulations on a polar grid to model the collapse of a 1 $M_\odot$ gas cloud of initially uniform density. Their inner radial boundary is an outflow boundary condition set at 6.7 au, which is the same radius as our sink particles. They varied several parameters including magnetic field strength, cosmic ionization rate, the grain model and which non-ideal MHD terms were included. In strong magnetic fields, they found that discs did not form, even when Ohmic resistivity and ambipolar diffusion were included. For weak magnetic fields, they found small discs normally formed at early times, but later dissipated due to powerful outflows.

Both Tomida et al. (2015) and Tsukamoto et al. (2015a) modelled the collapse of a gas cloud in 3D, and both studies compared three models using a strong magnetic field, $\mu_0 \approx 4$: ideal MHD, Ohmic-only, Ohmic+ambipolar. Tomida et al. (2015) initialized their gas cloud as an unstabilized, rotating 1 $M_\odot$ Bonner–Ebert sphere; their simulations are performed on a nested grid, and includes radiative transfer. Tsukamoto et al. (2015a) used a radiative SPMHD code without sink particles, initializing their 1 $M_\odot$ gas cloud as an isothermal uniform gas sphere. Both of these models used a different initial radius than our cloud, thus the absolute initial magnetic field strength is different in each study.

Qualitatively, the studies agree that strong magnetic fields in ideal MHD models efficiently transport angular momentum and prevent the formation of a disc. By adding Ohmic resistivity, Tomida et al.

(2015) form a small disc simultaneous with the formation of the protostellar core. When ambipolar diffusion is also included, the disc forms prior to the formation of the protostellar core, and at the end of the first hydrostatic core phase, the disc radius is $r \approx 5$ au. They predict their disc will continue to grow, although it is already massive enough to form non-axisymmetric structures and possibly fragment. Tsukamoto et al. (2015a) form an $r \approx 1$ au disc just after the formation of the protostellar core in both of their models that include non-ideal MHD terms.

Caution must be used when comparing our models to previously published studies, since our sink particle has a radius of 6.7 au, thus we are unable to track discs smaller than this; moreover, discs with radii only slightly larger than this may be artificially created as a result of the sink particle's interaction with the nearby gas. Our definition of 'in the disc' (where the only requirement is $\rho_{\rm gas} > \rho_{\rm disc,\,min}$) likely allows for different size of discs to be reported for similar simulations. After the formation of the sink particle at in our $\mu_0 = 5$ models (excluding the Hall-only and non-ideal MHD models that are initialized with $\boldsymbol{B}_0 \cdot \boldsymbol{\Omega}_0 < 0$), the high-density gas is accreted on to the sink particle, leaving the systems devoid of any disc-like object. This lack of disc agrees with the other studies. In the high-resolution version of our Ohmic-only model, a disc does reform prior to the end of the simulation at $t = 1.21\,t_{\rm ff}$. The disc mass is low, comprising ∼6 per cent of the star+disc system mass.

5 SUMMARY AND CONCLUSION

We have presented a suite of simulations studying the effect of non-ideal MHD on the formation of circumstellar discs. Our models were initialized as a 1 $M_\odot$, spherically symmetric, rotating molecular cloud core with a magnetic field threaded vertically through it. We followed the gravitational collapse of the core until shortly after the formation of the first hydrostatic core using a barotropic equation of state. We tested the impact of each non-ideal MHD term (Ohmic resistivity, Hall effect and ambipolar diffusion) both independently and together. We further tested the effect of the initial mass-to-flux ratio μ_0, the direction of the seeded vertical magnetic field with respect to the axis of rotation, the cosmic ray ionization rate ζ and resolution. All of the simulations were performed using the SPMHD code PHANTOM, including self-gravity. Our key results are as follows.

(i) *Ideal MHD*: we performed simulations using ideal MHD with $\mu_0 = \infty$, 10, 7.5 and 5. As in PB07, stronger magnetic fields (smaller values of μ_0) yielded smaller and less massive discs. A bipolar outflow was launched shortly after a free-fall time in the magnetic models, with faster and more collimated outflows being launched in the models with stronger magnetic fields.

(ii) *Non-Ideal MHD*: for $\mu_0 = 10$, 7.5 and 5, we modelled the collapse using all three non-ideal MHD terms. For $\boldsymbol{B}_0 \cdot \boldsymbol{\Omega}_0 > 0$, the non-ideal MHD models yielded smaller discs than their ideal MHD counterparts, but yielded larger discs when initialized with $\boldsymbol{B}_0 \cdot \boldsymbol{\Omega}_0 < 0$. For $\mu_0 = 5$, we modelled the collapse using each effect separately, and used both signs of $\boldsymbol{B}_0 \cdot \boldsymbol{\Omega}_0$ for models that included the Hall effect. Discs did not form in any of the models initialized with $\boldsymbol{B}_0 \cdot \boldsymbol{\Omega}_0 > 0$. At all magnetic field strengths, the evolution of the system is dependent on the Hall effect and the sign of $\boldsymbol{B}_0 \cdot \boldsymbol{\Omega}_0$.

(iii) *Outflows*: we found an anticorrelation between the size and speed of the outflow and the size of the disc. That is, outflows carry away angular momentum and this hinders the formation of discs.

(iv) *Direction of the magnetic field*: we modelled the Hall-only and non-ideal MHD models using both signs of $\boldsymbol{B}_0 \cdot \boldsymbol{\Omega}_0$. For $\boldsymbol{B}_0 \cdot \boldsymbol{\Omega}_0 < 0$, the Hall effect resisted the momentum transport, and large discs formed. In the Hall-only model with $\mu_0 = 5$, an $r \approx 38$ au disc formed. In the non-ideal MHD model, an $r \approx 13$ au disc formed. In both models, counter-rotating envelopes formed at $r \in (90, 150)$ and $\gtrsim 150$ au, respectively.

(v) *Cosmic ray ionization rate*: our models are relatively insensitive to the cosmic ray ionization rate. The exceptions are the models that include the Hall effect and are initialized with $\boldsymbol{B}_0 \cdot \boldsymbol{\Omega}_0 < 0$, in which larger and more massive discs form in the models with lower cosmic ionization rates.

In the presence of strong magnetic fields, Ohmic resistivity and ambipolar diffusion cannot solve the magnetic braking catastrophe; as in ideal MHD models, large discs cannot form. However, the Hall effect with $\boldsymbol{B}_0 \cdot \boldsymbol{\Omega}_0 < 0$ can solve the magnetic braking catastrophe, allowing rotationally supported discs to form. Thus, the direction of the magnetic field with respect to the rotation axis is important (e.g. Wardle & Ng 1999), as found in Krasnopolsky et al. (2011) and Braiding & Wardle (2012b) and confirmed in our study. Larger and more massive discs form for $\boldsymbol{B}_0 \cdot \boldsymbol{\Omega}_0 < 0$, while catastrophic magnetic braking may occur for $\boldsymbol{B}_0 \cdot \boldsymbol{\Omega}_0 > 0$. Our results agree with the conclusions found in Tsukamoto et al. (2015b).

As discussed in Braiding & Wardle (2012a), targeted observations with telescopes such as Atacama Large Millimetre/Sumbillimetre Array (ALMA) should be able to determine the direction of the magnetic field with respect to the rotation axis of discs around newly forming stars. Our results on the Hall effect suggest that a correlation between $\boldsymbol{B}_0 \cdot \boldsymbol{\Omega}_0$ and disc size should be observed.

ACKNOWLEDGEMENTS

We thank the referee for a prompt and thorough review, whose comments resulted in the improved quality of this manuscript. This work was funded by an Australian Research Council (ARC) Discovery Projects Grant (DP130102078), including a Discovery International Award funding MRB's sabbatical at Monash. DJP is funded by ARC Future Fellowship FT130100034. MRB also acknowledges support from the European Research Council under the European Community's Seventh Framework Programme (FP7/2007- 2013 grant agreement no. 339248). We would like to thank Mark Wardle for helpful discussions and clarifications. This work was supported by resources on the gSTAR national facility at Swinburne University of Technology. gSTAR is funded by Swinburne and the Australian Government's Education Investment Fund. For the column density figures, we used SPLASH (Price 2007).

REFERENCES

Alexiades V., Amiez G., Gremaud P.-A., 1996, Commun. Numer. Methods Eng., 12, 31
Allen A., Li Z.-Y., Shu F. H., 2003, ApJ, 599, 363
Asplund M., Grevesse N., Sauval A. J., Scott P., 2009, ARA&A, 47, 481
Bai X.-N., 2014, ApJ, 791, 137
Bai X.-N., 2015, ApJ, 798, 84
Bate M. R., Burkert A., 1997, MNRAS, 288, 1060
Bate M. R., Bonnell I. A., Price N. M., 1995, MNRAS, 277, 362
Bate M. R., Tricco T. S., Price D. J., 2014, MNRAS, 437, 77
Børve S., Omang M., Trulsen J., 2001, ApJ, 561, 82
Børve S., Omang M., Trulsen J., 2004, ApJS, 153, 447
Bourke T. L., Myers P. C., Robinson G., Hyland A. R., 2001, ApJ, 554, 916
Braiding C. R., Wardle M., 2012a, MNRAS, 422, 261
Braiding C. R., Wardle M., 2012b, MNRAS, 427, 3188
Bürzle F., Clark P. C., Stasyszyn F., Dolag K., Klessen R. S., 2011, MNRAS, 417, L61
Choi E., Kim J., Wiita P. J., 2009, ApJS, 181, 413

Commerçon B., Hennebelle P., Audit E., Chabrier G., Teyssier R., 2010, A&A, 510, L3
Commerçon B., Teyssier R., Audit E., Hennebelle P., Chabrier G., 2011, A&A, 529, A35
Crutcher R. M., 1999, ApJ, 520, 706
Dapp W. B., Basu S., 2010, A&A, 521, L56
Dapp W. B., Basu S., Kunz M. W., 2012, A&A, 541, A35
Draine B. T., 1980, ApJ, 241, 1021
Duffin D. F., Pudritz R. E., 2009, ApJ, 706, L46
Dunham M. M., Chen X., Arce H. G., Bourke T. L., Schnee S., Enoch M. L., 2011, ApJ, 742, 1
Falle S. A. E. G., 2003, MNRAS, 344, 1210
Fujii Y. I., Okuzumi S., Inutsuka S.-i., 2011, ApJ, 743, 53
Gafton E., Rosswog S., 2011, MNRAS, 418, 770
Galli D., Lizano S., Shu F. H., Allen A., 2006, ApJ, 647, 374
Heiles C., Crutcher R., 2005, in Wielebinski R., Beck R., eds, Lecture Notes in Physics, Vol. 664, Cosmic Magnetic Fields. Springer-Verlag, Berlin, p. 137
Hennebelle P., Ciardi A., 2009, A&A, 506, L29
Hennebelle P., Fromang S., 2008, A&A, 477, 9
Joos M., Hennebelle P., Ciardi A., Fromang S., 2013, A&A, 554, A17
Keith S. L., Wardle M., 2014, MNRAS, 440, 89
Krasnopolsky R., Li Z.-Y., Shang H., 2010, ApJ, 716, 1541
Krasnopolsky R., Li Z.-Y., Shang H., 2011, ApJ, 733, 54
Larson R. B., 1969, MNRAS, 145, 271
Lewis B. T., Bate M. R., Price D. J., 2015, MNRAS, 451, 288
Li Z.-Y., Krasnopolsky R., Shang H., 2011, ApJ, 738, 180
Li H.-b., Fang M., Henning T., Kainulainen J., 2013, MNRAS, 436, 3707
Li Z.-Y., Krasnopolsky R., Shang H., Zhao B., 2014, ApJ, 793, 130
Lindberg J. E. et al., 2014, A&A, 566, A74
Liu B., Goree J., Nosenko V., Boufendi L., 2003, Phys. Plasmas, 10, 9
Mac Low M.-M., Norman M. L., Konigl A., Wardle M., 1995, ApJ, 442, 726
Machida M. N., Tomisaka K., Matsumoto T., 2004, MNRAS, 348, L1
Machida M. N., Matsumoto T., Hanawa T., Tomisaka K., 2006, ApJ, 645, 1227
Machida M. N., Inutsuka S.-i., Matsumoto T., 2008a, ApJ, 676, 1088
Machida M. N., Tomisaka K., Matsumoto T., Inutsuka S.-i., 2008b, ApJ, 677, 327
Machida M. N., Inutsuka S.-I., Matsumoto T., 2011, PASJ, 63, 555
Machida M. N., Inutsuka S.-i., Matsumoto T., 2014, MNRAS, 438, 2278
Masunaga H., Inutsuka S.-i., 2000, ApJ, 531, 350
Mellon R. R., Li Z.-Y., 2008, ApJ, 681, 1356
Mellon R. R., Li Z.-Y., 2009, ApJ, 698, 922
Mestel L., Spitzer L., Jr, 1956, MNRAS, 116, 503
Monaghan J. J., 2002, MNRAS, 335, 843
Morales Ortiz J. L., Ceccarelli C., Lis D. C., Olmi L., Plume R., Schilke P., 2014, A&A, 563, A127
Morris J. P., 1996, PASA, 13, 97
Mouschovias T. C., Spitzer L., Jr, 1976, ApJ, 210, 326
Myers P. C., Goodman A. A., 1988, ApJ, 326, L27
Nakano T., Umebayashi T., 1986, MNRAS, 218, 663
Nakano T., Nishi R., Umebayashi T., 2002, ApJ, 573, 199
O'Sullivan S., Downes T. P., 2006, MNRAS, 366, 1329
Osterbrock D. E., 1961, ApJ, 134, 270
Pandey B. P., Wardle M., 2008, MNRAS, 385, 2269
Pinto C., Galli D., 2008, A&A, 484, 17
Pollack J. B., Hollenbach D., Beckwith S., Simonelli D. P., Roush T., Fong W., 1994, ApJ, 421, 615
Price D. J., 2007, PASA, 24, 159
Price D. J., 2010, MNRAS, 401, 1475
Price D. J., 2012, J. Comput. Phys., 231, 759
Price D. J., Bate M. R., 2007, MNRAS, 377, 77 (PB07)
Price D. J., Federrath C., 2010, MNRAS, 406, 1659
Price D. J., Monaghan J. J., 2004, MNRAS, 348, 123
Price D. J., Monaghan J. J., 2005, MNRAS, 364, 384
Price D. J., Monaghan J. J., 2007, MNRAS, 374, 1347
Price D. J., Tricco T. S., Bate M. R., 2012, MNRAS, 423, L45
Sano T., Stone J. M., 2002, ApJ, 570, 314
Santos-Lima R., de Gouveia Dal Pino E. M., Lazarian A., 2012, ApJ, 747, 21
Santos-Lima R., de Gouveia Dal Pino E. M., Lazarian A., 2013, MNRAS, 429, 3371
Seifried D., Banerjee R., Klessen R. S., Duffin D., Pudritz R. E., 2011, MNRAS, 417, 1054
Seifried D., Banerjee R., Pudritz R. E., Klessen R. S., 2012, MNRAS, 423, L40
Seifried D., Banerjee R., Pudritz R. E., Klessen R. S., 2013, MNRAS, 432, 3320
Shu F. H., Galli D., Lizano S., Cai M., 2006, ApJ, 647, 382
Springel V., Hernquist L., 2002, MNRAS, 333, 649
Tassis K., Mouschovias T. C., 2007, ApJ, 660, 388
Tobin J. J. et al., 2015, ApJ, 805, 125
Tomida K., Tomisaka K., Matsumoto T., Hori Y., Okuzumi S., Machida M. N., Saigo K., 2013, ApJ, 763, 6
Tomida K., Okuzumi S., Machida M. N., 2015, ApJ, 801, 117
Tomisaka K., 1998, ApJ, 502, L163
Tomisaka K., 2002, ApJ, 575, 306
Tomisaka K., Machida M. N., Matsumoto T., 2004, Ap&SS, 292, 309
Tricco T. S., Price D. J., 2012, J. Comput. Phys., 231, 7214
Tricco T. S., Price D. J., 2013, MNRAS, 436, 2810
Tsukamoto Y., Iwasaki K., Inutsuka S.-i., 2013, MNRAS, 434, 2593
Tsukamoto Y., Iwasaki K., Okuzumi S., Machida M. N., Inutsuka S., 2015a, MNRAS, 452, 278
Tsukamoto Y., Iwasaki K., Okuzumi S., Machida M. N., Inutsuka S., 2015b, ApJ, 810, L26
Umebayashi T., Nakano T., 1980, PASJ, 32, 405
Umebayashi T., Nakano T., 1990, MNRAS, 243, 103
Umebayashi T., Nakano T., 2009, ApJ, 690, 69
Wardle M., 2007, Ap&SS, 311, 35
Wardle M., Ng C., 1999, MNRAS, 303, 239 (WN99)
Wurster J., Price D., Ayliffe B., 2014, MNRAS, 444, 1104

APPENDIX A: EQUATION OF STATE

A1 Discontinuous temperatures

The barotropic equation of state given in (5) yields a continuous pressure, shown as the red curve in Fig. A1. The local sound speed

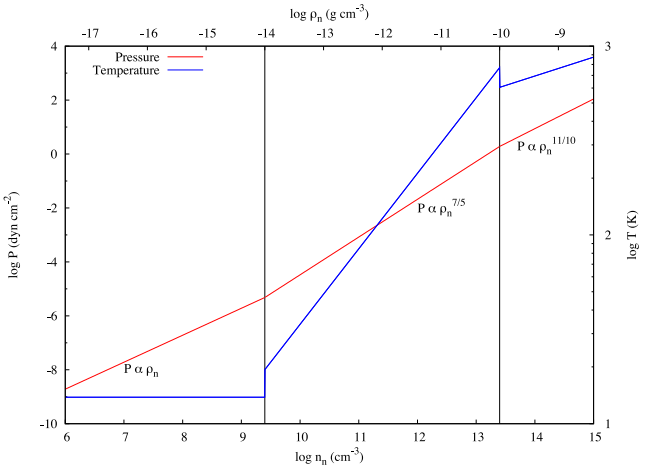

Figure A1. Pressure (red) and temperature (blue) resulting from the barotropic equation of state (equation 5). The vertical lines are the threshold densities, ρ_d and ρ_c. The pressure is a continuous function of density, while temperature is discontinuous at the threshold densities.

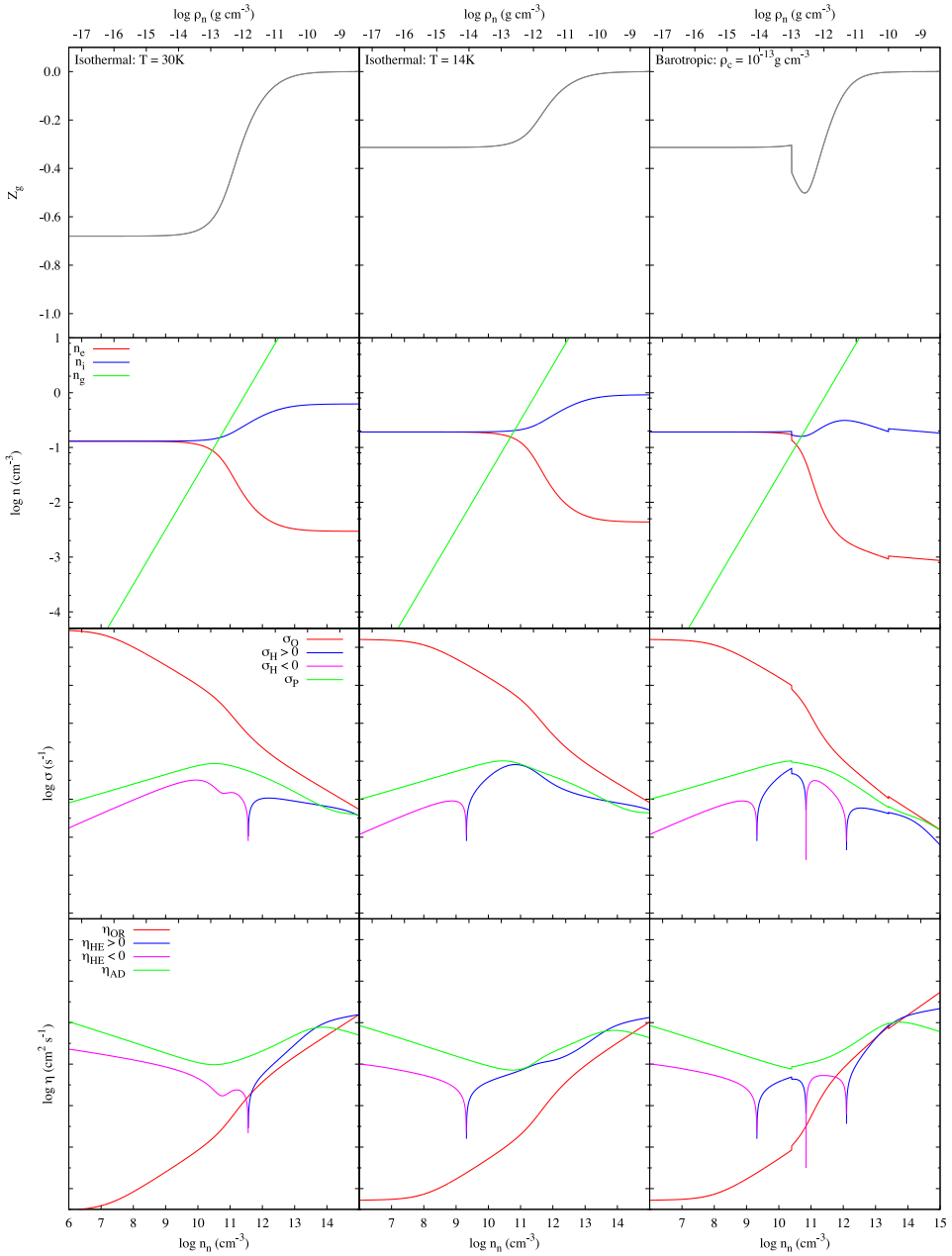

Figure A2. Top to bottom: grain charge, number densities, conductivities and resistivity coefficients for the isothermal equations of state. In all cases, $\zeta = 10^{-17}$ s^{-1}. The top ticks on each panel correspond to mass density (top scale), and the bottom ticks correspond to number density (bottom scale). This is comparable to Fig. 1. Left-hand column: isothermal equation of state with $T = 30$ K to match Wardle & Ng (1999). The middle two panels are directly comparable to their Fig. 1. Middle column: isothermal equation of state with $T = 14$ K to match our temperature for $\rho < \rho_c = 10^{-14}$ g cm^{-3}. Right-hand column: barotropic equation of state with $\rho_c = 10^{-13}$ g cm^{-3}.

is given by

$$c_s = \sqrt{\gamma \frac{P}{\rho}}, \tag{A1}$$

where

$$\gamma = \begin{cases} 1; & \rho < \rho_c, \\ 7/5; & \rho_c \leq \rho < \rho_d, \\ 11/10; & \rho \geq \rho_d. \end{cases} \tag{A2}$$

This local sound speed is converted into temperature using

$$T = \frac{c_s^2 \mu m_p}{k_B}, \tag{A3}$$

where μ is the mean molecular mass, m_p is the proton mass and k_B is the Boltzmann constant. It is this temperature that is used in the ionization calculations, and is shown as the blue curve in Fig. A1. The discontinuities in temperature at the threshold densities are thus responsible for the discontinuities in grain charge, number densities, conductivities and resistivities in our test cases in Sections 2.2 and 2.3. Future work will test the effect of modifying (A3) to be a continuous function of n_n.

A2 Isothermal equation of state

As shown in Sections 2.2 and 2.3, the grain charge, species number densities, conductivities and resistivity coefficients are dependent on the value of ζ. Where possible, we have obtained the remaining parameters from experimental values, however the specific values will necessarily affect the results. In this appendix, we will briefly discuss the effect of the equation of state. For our simulations, we have chosen a barotropic equation of state (cf. equation 5) to mimic the expected equation of state in a star formation scenario without requiring a full radiative treatment. In Wardle & Ng (1999, herein WN99), an isothermal equation of state is used with $T = 30$ K. In the first column of Fig. A2, we plot the grain charge, number densities of the charges species, conductivities, σ and resistivity coefficients, η for the isothermal equation of state. For $\rho < \rho_c = 10^{-14}$ g cm^{-3}, our equation of state assumes an isothermal temperature of $T = 14$ K, which is plotted in the second column.

At $T = 30$ K, our calculation of number densities, specifically the grain number density, varies from WN99, who obtain their values from Umebayashi & Nakano (1990). With the isothermal equation of state, the ion and electron number densities at $n_n \sim 10^{15}$ cm^{-3} agree within a factor of $\sim$2 and n_i and n_e diverge at approximately the same neutral number density. For low densities, our ion and electron number densities are constant whereas they slightly decline in WN99. This discrepancy is likely a result of the grain charge: our grain charge is given in the top panel, while WN99's charge is ± 1. Given the interdependence of number density, temperature and a grain charge in our algorithms, we can choose two values and then must self-consistently calculate the third.

The Hall conductivity is the conductivity that is most modified by the equation of state. By using an isothermal equation of state, the change of sign is at $n_n \approx 3.6 \times 10^{11}$ cm^{-3} compared to $\approx 1.5 \times 10^{12}$ cm^{-3} for the barotropic equation of state. As for $\zeta = 10^{-17}$ s^{-1}, the isothermal case does not have a second change of sign at lower densities. The Pedersen conductivity is similar for both equations of state. The Ohmic conductivity can vary by a factor of 10, and the conductivity calculated with the isothermal equation of state is in better agreement to the values presented in WN99.

A3 Barotropic equation of state with $\rho_c = 10^{-13}$ g cm^{-3}

In the right-hand column of Fig. A2, we plot the grain charge, number densities of the charges species, conductivities, σ and resistivity coefficients, η for the barotropic equation of state using $\rho_c = 10^{-13}$ g cm^{-3}. The result is similar to Fig. 1, where $\rho_c = 10^{-14}$ g cm^{-3}. With the exception of grain charge, σ_H and η_H, the values calculated by both values of ρ_c are typically differ by less than a factor of 2. The grain charge does not become as negative with $\rho_c = 10^{-13}$ g cm^{-3}. There is a third density at which $\sigma_H, \eta_H \to 0$; moreover, these values remain negative below $n_n \approx 1.5 \times 10^{12}$ cm^{-3}.

APPENDIX B: THE MODIFIED HALL PARAMETER

The Hall parameter is defined in (22), and our modified parameters are given in (23). The conductivities, σ, and coefficients, η, are unaffected by the form of the Hall parameter for $n_n \gtrsim 10^9$ cm^{-3}. Below this density, the values of the conductivities and coefficients calculated with the modified Hall parameters begin to diverge from their unmodified counterparts. The maximum difference between the versions of σ_H, σ_P, η_{HE} and η_{AD} is 1.5 per cent, occurring at the minimum density tested, $n_n = 10^6$ cm^{-3}. Both σ_O and η_{OR} yield larger divergences, as plotted in the top panel of Fig. B1. At $n_n = 10^6$ cm^{-3}, the two forms of σ_O and η_{OR} differ by a factor of $\sim$12. Although the modified η_{OR} has a larger value than its unmodified counterpart, both modified and unmodified values are more than seven orders of magnitude lower than the resistivities for the Hall effect or ambipolar diffusion. Thus, the choice of the Hall parameter is not important for star formation. For consistency with the η_{OR} presented in Pandey & Wardle (2008) and Keith & Wardle (2014), we use the modified versions.

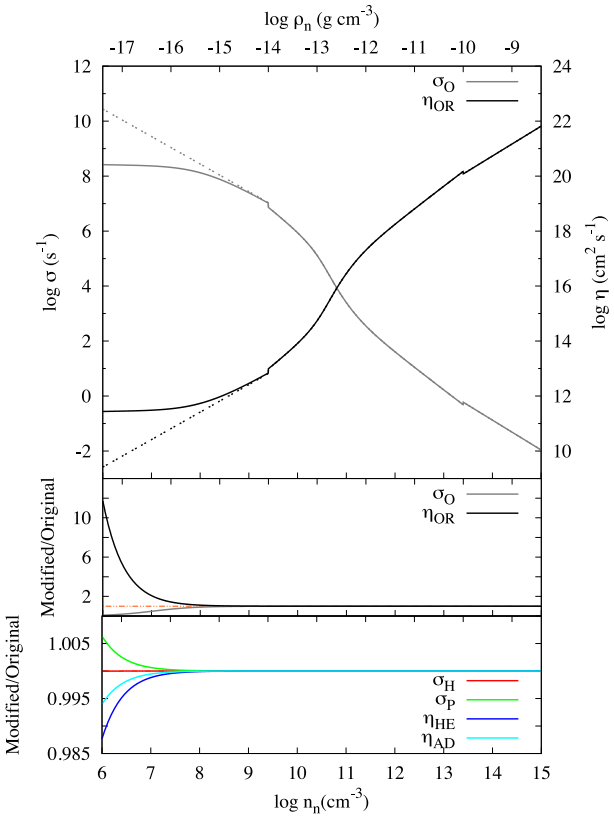

Figure B1. Top: Ohmic conductivity and resistivity, using the modified Hall parameters used in all calculations (solid) and the original Hall parameters (dashed). In all cases, $\zeta = 10^{-17}$ s^{-1}. The vertical range is different than in Figs 1 and A2 to avoid truncating the curves. Middle and bottom: ratios of the conductivities and resistivities calculated using the modified Hall parameters to that using the original Hall parameters. Note that the bottom two panels have different vertical scales from one another. The top ticks on each panel correspond to mass density (top scale), and the bottom ticks correspond to number density (bottom scale). At the lower end of the given number density range, Ohmic conductivity and resistivity differ significantly depending on the Hall parameters; the remaining conductivities and resistivities are relatively unaffected by the form of the Hall parameters. At the densities where the choice of the Hall parameter affects the Ohmic conductivity and resistivity, Ohmic resistivity is the weakest non-ideal MHD effect by at least seven orders of magnitude.

APPENDIX C: VERIFICATION OF NUMERICAL METHODS

C1 The hall effect

The algorithm that governs ambipolar diffusion was thoroughly tested in Wurster et al. (2014). The same general algorithm governs

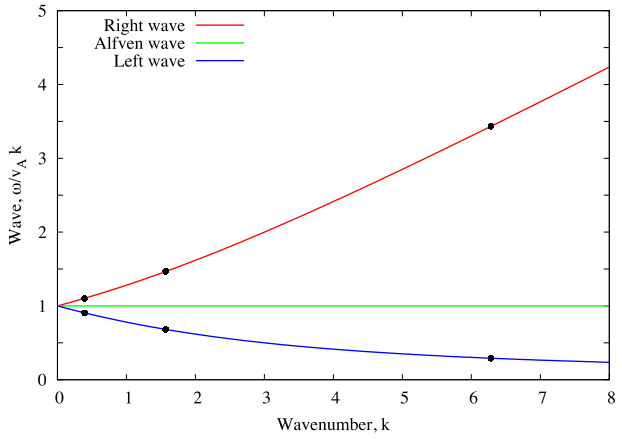

Figure C1. Dispersion relation for the left- and right-circularly polarized wave, corresponding to $\eta_{\rm HE} < 0$ and >0, respectively. The solid circles are the numerically calculated phase velocities.

the Hall effect, but given its non-diffusive behaviour, we verify the algorithm here.

C1.1 Wave test

As in Sano & Stone (2002), we test our algorithm by comparing the numerically measured phase velocity with the linear dispersion relation, which is given by

$$\left(\omega^2 - v_{\rm A}^2 k^2\right)^2 = \eta_{\rm HE}^2 k^4 \omega^2, \tag{C1}$$

where ω is the angular frequency of the wave and k is the wavenumber. In Fig. C1, we plot the analytical dispersion relation for the left- and right-circularly polarized wave, which correspond to $\eta_{\rm HE} < 0$ and $\eta_{\rm HE} > 0$, respectively. We also plot our numerical results at fixed wavenumbers and constant Hall resistivities. Our numerical results agree with the analytical prediction within 1 per cent.

C1.2 Standing shock test

As in Falle (2003) and O'Sullivan & Downes (2006), we test our algorithm against the 1D isothermal steady-state equations for the strong Hall effect regime. The analytical result is derived by setting $\frac{\partial}{\partial t} = 0$ and $\frac{\rm d}{{\rm d}y} = \frac{\rm d}{{\rm d}z} = 0$ in (1)–(3). Assuming $\frac{{\rm d}B_{\rm x}}{{\rm d}x} = 0$, the steady state can be represented with the following two, coupled ordinary differential equations,

$$\frac{{\rm d}B_{\rm y}}{{\rm d}x} = \frac{M_1 R_{22} - M_2 R_{12}}{R_{11} R_{22} - R_{21} R_{12}}, \tag{C2a}$$

$$\frac{{\rm d}B_{z}}{{\rm d}x} = \frac{M_1 R_{21} - M_2 R_{11}}{R_{12} R_{21} - R_{22} R_{11}}, \tag{C2b}$$

where each term on the right-hand side can be written in terms of only $\boldsymbol{B}$:

$$M_1 = v_{\rm x} B_{\rm y} - v_{\rm x,0} B_{\rm y,0} + v_{\rm y,0} B_{\rm x,0} - v_{\rm y} B_{\rm x,0}, \tag{C3a}$$

$$M_2 = v_{\rm x} B_{\rm z} - v_{\rm x,0} B_{\rm z,0} + v_{\rm z,0} B_{\rm x,0} - v_{\rm z} B_{\rm x,0}, \tag{C3b}$$

$$R_{11} = \left(\eta_{\rm OR}^{\rm c} - \eta_{\rm AD}^{\rm c}\right) \frac{B_{\rm z}^2}{B^2} + \eta_{\rm AD}^{\rm c}, \tag{C3c}$$

$$R_{12} = \left(\eta_{\rm AD}^{\rm c} - \eta_{\rm OR}^{\rm c}\right) \frac{B_{\rm y} B_{\rm z}}{B^2} + \eta_{\rm HE}^{\rm c} \frac{B_{\rm x}}{B}, \tag{C3d}$$

$$R_{21} = \left(\eta_{\rm AD}^{\rm c} - \eta_{\rm OR}^{\rm c}\right) \frac{B_{\rm y} B_{\rm z}}{B^2} - \eta_{\rm HE}^{\rm c} \frac{B_{\rm x}}{B}, \tag{C3e}$$

$$R_{22} = \left(\eta_{\rm OR}^{\rm c} - \eta_{\rm AD}^{\rm c}\right) \frac{B_{\rm y}^2}{B^2} + \eta_{\rm AD}^{\rm c}. \tag{C3f}$$

Once the magnetic field is known, then the velocities are given by

$$v_{\rm x} = \frac{1}{2Q}\left(K_{\rm x} - \frac{B^2}{2} - \sqrt{\left(K_{\rm x} - \frac{B^2}{2}\right)^2 - 4c_{\rm s}^2 Q^2}\right), \tag{C4a}$$

$$v_{\rm y} = \left(K_{\rm y} + B_{\rm x} B_{\rm y}\right)/Q, \tag{C4b}$$

$$v_{\rm z} = \left(K_{\rm z} + B_{\rm x} B_{\rm z}\right)/Q, \tag{C4c}$$

where $c_{\rm s}$ is the isothermal sound speed, and $K_{\rm x}$, $K_{\rm y}$, $K_{\rm z}$ and $Q = \rho v_{\rm x}$ are constants which can be calculated from the initial conditions. The resistivities, $\eta^{\rm c}$, are semiconstant, given by

$$\eta_{\rm OR}^{\rm c} = C_{\rm OR}, \tag{C5a}$$

$$\eta_{\rm HE}^{\rm c} = C_{\rm HE} B, \tag{C5b}$$

$$\eta_{\rm AD}^{\rm c} = C_{\rm AD} \frac{B^2}{\rho} \equiv \frac{v_{\rm A}^2}{\gamma_{\rm AD} \rho_{\rm ion}}, \tag{C5c}$$

where $C_{\rm OR}$, $C_{\rm HE}$ and $C_{\rm AD}$ are constants, $\gamma_{\rm AD}$ is the collisional coupling constant between ions and neutrals and $\rho_{\rm ion}$ is the ion density. The final term of (C5c) matches the form presented in Wurster et al. (2014).

For our numerical test, we set up the shock where the values for the left- and right-hand sides are given by $(\rho_0, P_0, v_{\rm x,0}, v_{\rm y}, v_{\rm z,0}, B_{\rm y,0}, B_{\rm z,0}) = (1.7942, 0.017\,942, -0.9759, -0.6561, 0.0, 1.748\,85, 0.0)$ and $(1.0, 0.01, -1.751, 0.0, 0.0, 0.6, 0.0)$, respectively. The x-magnetic field is constant at $B_{\rm x} = 1$, and the isothermal sound speed is $c_{\rm s} = 0.1$. The coefficients are $C_{\rm OR} = 1.12 \times 10^{-9}$, $C_{\rm HE} = -3.53 \times 10^{-2}$ and $C_{\rm AD} = 7.83 \times 10^{-3}$, thus this evolution will be dominated by the Hall effect.

The particles are set up on a closed-packed lattice with 512 particles in the x-direction on the left-hand side, and 12 and 13 particles in the y- and z-directions, respectively. Initializing this idealized test on a three-dimensional lattice will yield instabilities as the system evolves (Morris 1996); unlike the results presented in this paper, these particles are expected to evolve on the lattice, thus the regular shape will not be washed out. To minimize the instabilities, we use the $\mathcal{C}^4$ Wendland kernel.

The analytical and numerical results are plotted in Fig. C2. At any given position, the analytical and numerical solutions agree within 3 per cent. Similar results are obtained using different kernels and different initial lattice configurations.

C2 Super timestepping

We have implemented super timestepping into PHANTOM for both global and individual particle timesteps. In both cases, ${\rm d}t'_{\rm diff}$ is determined from the globally minimum $\min({\rm d}t_{\rm OR}, {\rm d}t_{\rm AD})$, while ${\rm d}t$ is either the globally or locally minimum $\min({\rm d}t_{\rm Courant}, {\rm d}t_{\rm HE})$ for global and individual timesteps, respectively.

We use the isothermal C-shock (Draine 1980) with individual timesteps to test the effectiveness of our super timestepping implementation. We include ambipolar diffusion with the semiconstant resistivity given in (C5c), setting $\gamma_{\rm AD} = 1$. Given our implementation of super timestepping, k is the only free parameter, where

Table C1. The results from the isothermal C-shock test using ambipolar diffusion with constant resistivity using $\gamma_{\rm AD} = 1$ and $\rho_{\rm ion}$ as listed in the first column. The results are presented for the final times of $t_{\rm final} = 14.5$ and $1.25\tau_{\rm AD}$ for $\rho_{\rm ion} = 10^{-5}$ and 10^{-6}, respectively. The rows with a dash listed for k are simulations without super timestepping. The third column is the total number of steps, where one step is defined as progressing time $\mathrm{d}\tau$. The fourth column is the runtime in hours, using individual timesteps and OpenMP on 12 nodes. The fifth column is total energy at $t_{\rm final}$, in code units. The sixth column is the sum of the density of each SPH particle that satisfies $\rho > \rho_0$. The seventh column is the maximum number of sub-steps required on any given $\mathrm{d}t$ after subdividing $\mathrm{d}t$ if required due to the signal velocity constraint. The eighth column is the maximum number of sub-steps used in the super timestepping algorithm, and the ninth column is its corresponding ν.

$\rho_{\rm ion}$	k	$N_{\rm total}$	Runtime (h)	$E_{\rm total}$ ($\times 10^{19}$ code)	$\sum(\rho > \rho_0)$ ($\times 10^{6}$ code)	$N'_{\rm max}$	$N_{\rm max}$	$\nu(N_{\rm max})$
10^{-5}	–	26 829	6.06	2.273	2.708	–	–	–
10^{-5}	0.30	17 588	6.05	2.274	2.705	4	4	1.73×10^{-1}
10^{-5}	0.60	13 238	4.88	2.276	2.677	3	3	6.47×10^{-2}
10^{-5}	0.90	12 199	4.83	2.277	2.696	3	3	9.72×10^{-3}
10^{-5}	0.99	11 551	4.55	2.277	2.696	3	3	8.67×10^{-4}
10^{-6}	–	142 203	24.50	2.4065	2.990	–	–	–
10^{-6}	0.30	37 456	21.56	2.4061	2.992	0	11	1.92×10^{-2}
10^{-6}	0.60	41 936	23.94	2.4062	2.992	30	9	7.07×10^{-3}
10^{-6}	0.90	44 706	25.39	2.4061	2.992	62	9	1.06×10^{-3}
10^{-6}	0.99	61 445	34.44	2.4061	2.992	393	23	1.44×10^{-5}

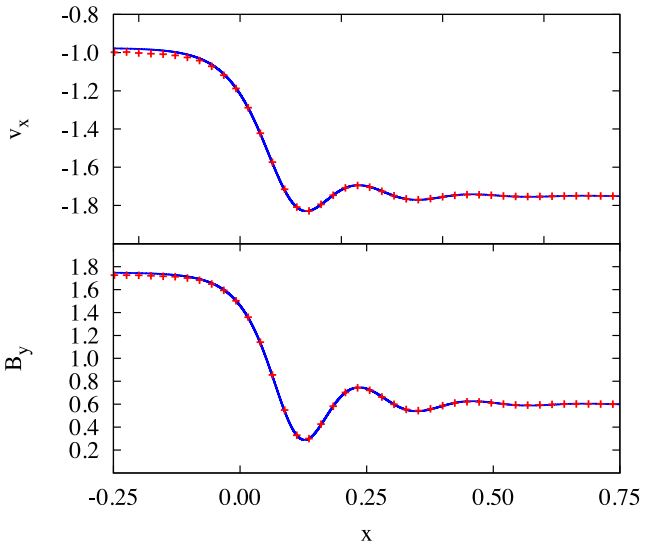

Figure C2. The analytical (solid line) and numerical (crosses) results for the isothermal standing shock. The initial conditions are given in the text. At any given position, the analytical and numerical solutions agree within 3 per cent.

a smaller k yields a larger N. Our tests are run using OpenMP on 12 nodes, and exclude Ohmic resistivity and the Hall effect.

Using $\rho_{\rm ion} = 10^{-5}$, we run the C-shock using four values of k, as well as a fiducial run without super timestepping. In Table C1, we summarize the results of these tests at $t_{\rm final} = 14.5\tau_{\rm AD}$, where $\tau_{\rm AD} = (\gamma_{\rm AD}\rho_{\rm ion})^{-1}$ is the characteristic time-scale for ambipolar diffusion.

In each of the models with super timestepping, the number of *real* steps (where one real step is defined as progressing time $\mathrm{d}t$) is 4576, which $\sim$5.9$\times$ lower than the number of real steps required without super timestepping. As expected, the *total* number of steps (where one step is defined as progressing time $\mathrm{d}\tau$) decreases for increasing k. The required number of sub-steps per step varies as the simulation evolves, hence the non-linear relation between the total number of steps and k. The maximum number of sub-steps is typically $N_{\rm max} = 3$; the corresponding ν is given in the final column of Table C1. At $t_{\rm final}$, the total energy of each model differs by less than 0.18 per cent. For a second comparison, we sum the density of each SPH particle i that satisfies $\rho_i > \rho_0 \equiv 1$; these sums differ by less than 0.45 per cent.

We urge caution when comparing the runtimes to the model without super timestepping. In this test, all of the particles have timesteps that are constrained by ambipolar diffusion. Thus, all particles are evolved with the super timestepping algorithm using the globally minimum $\mathrm{d}t_{\rm AD}$ and $\mathrm{d}t_{\rm Courant}$. Thus, in this model, the supertimestep algorithm essentially uses global timesteps. The model without super timestepping continues to optimize the individual timesteps; although more steps are required in total, not every particle is evolved on the shortest timestep, thus decreasing the wall time.

We have also tested our algorithm in the more extreme condition of $\rho_{\rm ion} = 10^{-6}$; the results are also presented in Table C1. Again, ambipolar diffusion was the limiting timestep for all particles, thus our super timestepping algorithm essentially used global timesteps. In this case, the large resistivity meant that large changes in the signal velocity occurred, hence our algorithm routinely decreased $\mathrm{d}t$ such that $\mathrm{d}\tau$ was never 'too large'. As expected, this occurred more frequently for larger k, thus smaller k led to a greater number of steps. Although super timestepping is not efficient under these conditions, we can be confident that our algorithm can successfully handle steep shocks since the total energies and summed densities of each model differ by less than 0.017 and 0.33 per cent, respectively. Further, given that the majority of the particles in the models presented in this paper are not constrained by Ohmic resistivity or ambipolar diffusion, our super timestepping algorithm continues to optimize the individual timesteps to decrease the runtime.

In the models presented in the paper, the number of steps taken by the supertimestep algorithm is typically less than 10, but a few iterations use upwards of 30 sub-steps; these correspond to $\nu = 2.26 \times 10^{-2}$ and 9.47×10^{-5}, respectively. Given the tests presented here, we are confident that our results are not negatively impacted by super timestepping.

This paper has been typeset from a TEX/LATEX file prepared by the author.